



# Comparative lithology and alteration mineral chemistry of host rocks at the Seabee Gold Operation, northern Saskatchewan, Canada: Implications for a connected orogenic gold-mineralizing system

D. Beaudin<sup>a</sup>, C.A. Partin<sup>a</sup>, K. Ansdell<sup>a,\*</sup>, P. Yang<sup>b</sup>

<sup>a</sup> Department of Geological Sciences, University of Saskatchewan, 114 Science Place, Saskatoon, SK S7N 5E2, Canada

<sup>b</sup> Department of Earth Sciences, University of Manitoba, 125 Dysart Road Winnipeg, Manitoba R3T 2N2, Canada

## ARTICLE INFO

### Keywords:

Orogenic gold  
Trans-Hudson orogen  
Glennie domain  
Alteration mineral assemblage  
Greenstone belt  
Structurally-controlled mineral deposit

## ABSTRACT

The Seabee Gold Operation, located in northern Saskatchewan, Canada, hosts the Santoy and Seabee gold deposits, as well as the Fisher property; the latter is an important exploration target. This gold mineralization is hosted in rocks of the Pine Lake greenstone belt that is within the Glennie domain of the larger Paleoproterozoic Trans-Hudson orogen. Mineralization is focused within shear zones, including the Santoy shear system that extends south onto the Fisher property. The role of ore-adjacent intrusions, systematics of gold mineralization, and relationship between the mineralization of the properties are largely undefined. In this study, hydrothermally-altered samples from locations along the Santoy shear system, namely the Santoy 7, Santoy Gap, and the Fisher property, were analyzed to identify and compare the mineralogical and geochemical characteristics related to sulfide-gold mineralization and associated alteration.

The altered host rocks primarily comprise upper greenschist to lower amphibolite-grade sheared metabasalt to chlorite-hornblende-biotite ± garnet schist, and intrusive rocks dominated by granodiorite and tonalite. These lithologies are cut by similar quartz vein generations and are associated with similar alteration assemblages and mineralization, including (i) *syn*-late-D<sub>3</sub> “distal” (~0.4 to 3 m wide) sericite-biotite-chlorite-clinzoisite ± albite, titanite to vein-adjacent coarse-grained diopside-K-feldspar-albite-actinolite ± apatite, titanite calc-silicate alteration, associated with main-stage Py<sub>2a</sub>, <sub>2b</sub>-Cpy<sub>2</sub>-Po<sub>1</sub>-Au (*syn*-late-D<sub>3</sub>) mineralization; (ii) remobilized, fracture-filling Py<sub>3</sub>-Po<sub>2</sub>-Cpy<sub>3</sub>-Au-BiTel (late-D<sub>3</sub>) mineralization within the calc-silicate assemblage; and (iii) early colloform Py<sub>1a</sub> (pre-*syn*-D<sub>3</sub>) and intrusion-hosted, inclusion-rich Py<sub>1b</sub> (pre-D<sub>3</sub>). Microprobe analyses reveal similar mineralogical trends between Fisher and Santoy alteration minerals typical of orogenic gold systems. Empirical geothermobarometric calculations of gold-associated vein-adjacent and vein-hosted chlorite and biotite exhibit orogenic-style formation conditions (~320–330 °C, 3 kbar, ~9 km depth). As such, these analyses suggest that the Fisher property and Santoy Mine Complex underwent inter-connected, multi-stage hydrothermal processes. These stages comprise (i) a potential early introduction of gold into the system closer to the timing of plutonism (Py<sub>1b</sub> magmatic-hydrothermal; pre-D<sub>1</sub>) or during the onset of gold mineralization (Py<sub>1a</sub>; orogenic; late-D<sub>2</sub> to early-*syn*-D<sub>3</sub>) during the evolution of the Reindeer zone; (ii) orogenic main-stage mineralization (*syn*-late-D<sub>3</sub>) concurrent with late- to post- collisional deformation throughout the Reindeer zone; and (iii) remobilization during continuous deformation (late-D<sub>3</sub>) where elevated cyclical fluid fluxes and higher fracture density at Santoy produced higher-grade mineralization.

## 1. Introduction

Orogenic gold mineralization within the Canadian extent of the Paleoproterozoic Trans-Hudson orogen is particularly abundant in the La Ronge-Lynn Lake belt and the Flin Flon-Glennie domains in the

provinces of Saskatchewan and Manitoba, Canada (Fig. 1; Corrigan et al., 2007, Morelli and MacLachlan, 2012, Lawley et al., 2020). In these domains, orogenic gold mineralization occurred from ca. 1.83 to 1.79 Ga during or after deformation associated with the collision between juvenile terranes and the Archean Hearne, Sask, and Superior

\* Corresponding author.

E-mail address: [kevin.ansdell@usask.ca](mailto:kevin.ansdell@usask.ca) (K. Ansdell).

<https://doi.org/10.1016/j.oregeorev.2024.105950>

Received 16 May 2023; Received in revised form 1 February 2024; Accepted 15 February 2024

Available online 24 February 2024

0169-1368/© 2024 The Author(s). Published by Elsevier B.V. This is an open access article under the CC BY-NC license (<http://creativecommons.org/licenses/by-nc/4.0/>).

cratons (Corrigan et al., 2007). However, mineralizing systems attributed to earlier geodynamic or magmatic settings during the evolution of these domains, may have also been present or overprinted. Relative to orogenic processes amidst greenstone belt evolution, preceding mineralizing processes have been identified in other Precambrian terranes, including (i) the input of magmatic fluids during *syn*-volcanic plutonism that may form early low-grade gold that is subsequently upgraded by orogenic gold systems (Meffre et al., 2016); (ii) the interaction of magmatic-hydrothermal fluids in the latter stages of an evolving greenstone belt during orogenesis (e.g., the Chalice deposit; Yilgarn craton, Bucci et al., 2004); and (iii) the formation of intrusion-related gold deposits, which are overprinted in an orogenic system (e.g., the Wasamac deposit, Abitibi greenstone belt; Mériaud and Jébrak, 2017). In addition, orogenic processes following the emplacement of intrusive bodies promotes the development of shear zones and fluid pathways at rheological contrasts between supracrustal-intrusion boundaries, facilitating orogenic gold mineralization (Groves et al., 2018, e.g. Granny Smith deposit, Yilgarn craton; Ojala et al., 1993). As such, these processes result in a distinct spatial association between intrusions and auriferous quartz veins; therefore, the origin of hydrothermal fluids and interaction between systems is critical to understanding their genesis.

Orogenic gold deposits typically form on a regional-scale during the terminal stages of accretionary and collisional orogens within a forearc or back-arc tectonic setting. These epigenetic deposits are hosted in lower metamorphic grade (e.g., greenschist facies) rocks, yield late- to

post-peak metamorphic timing of gold deposition, and show structurally-controlled mineralization (Groves et al., 1998). Orogenic gold deposits form by hydrothermal processes involving either metamorphic or subcrustal fluids during orogenic events, which propagate up crustal-scale structures and precipitate gold at higher levels in the crust (~4–15 km) (Groves, 1993, Kerrich and Cassidy, 1994, Goldfarb et al., 2005). These fluids tend to (i) be reduced, near neutral, moderate temperature ( $350 \pm 50 \text{ }^\circ\text{C}$ ), low-salinity,  $\text{H}_2\text{O-CO}_2 \pm \text{CH}_4 \pm \text{N}_2$  hydrothermal fluids, characteristic of low-sulfidation systems (Groves et al., 1998); (ii) transport gold as a bisulfide complex, creating deposits with Au-Ag  $\pm$  As, Sb, Bi, Te metal signatures; and (iii) deposit native gold within structurally controlled quartz-carbonate veins from phase separation, or as disseminated gold and minor sulfide-bound gold in wall rock from fluid-rock sulfidation reactions (Sibson et al., 1988, Groves et al., 1998, 2018; Cox, 1999). Intrusion-related gold systems within greenstone belts are considered local-scale magmatic-hydrothermal systems, with a genetic association between intermediate to felsic intrusions and mineralization (Sillitoe and Thompson, 1998, Dubé and Mercier-Langevin, 2015). In these systems intrusive magmas propagate to higher levels in the crust via fault structures and exsolve a metal-bearing fluid phase upon crystallization, which can interact with surrounding country rock and structures (Robert, 2001, Dubé and Mercier-Langevin, 2015). In contrast to orogenic systems, these magmatic fluids tend to be oxidized, saline, hot (~500 °C), and have a moderate-high CO<sub>2</sub> content (Sillitoe and Thompson, 1998, De Souza et al., 2019).

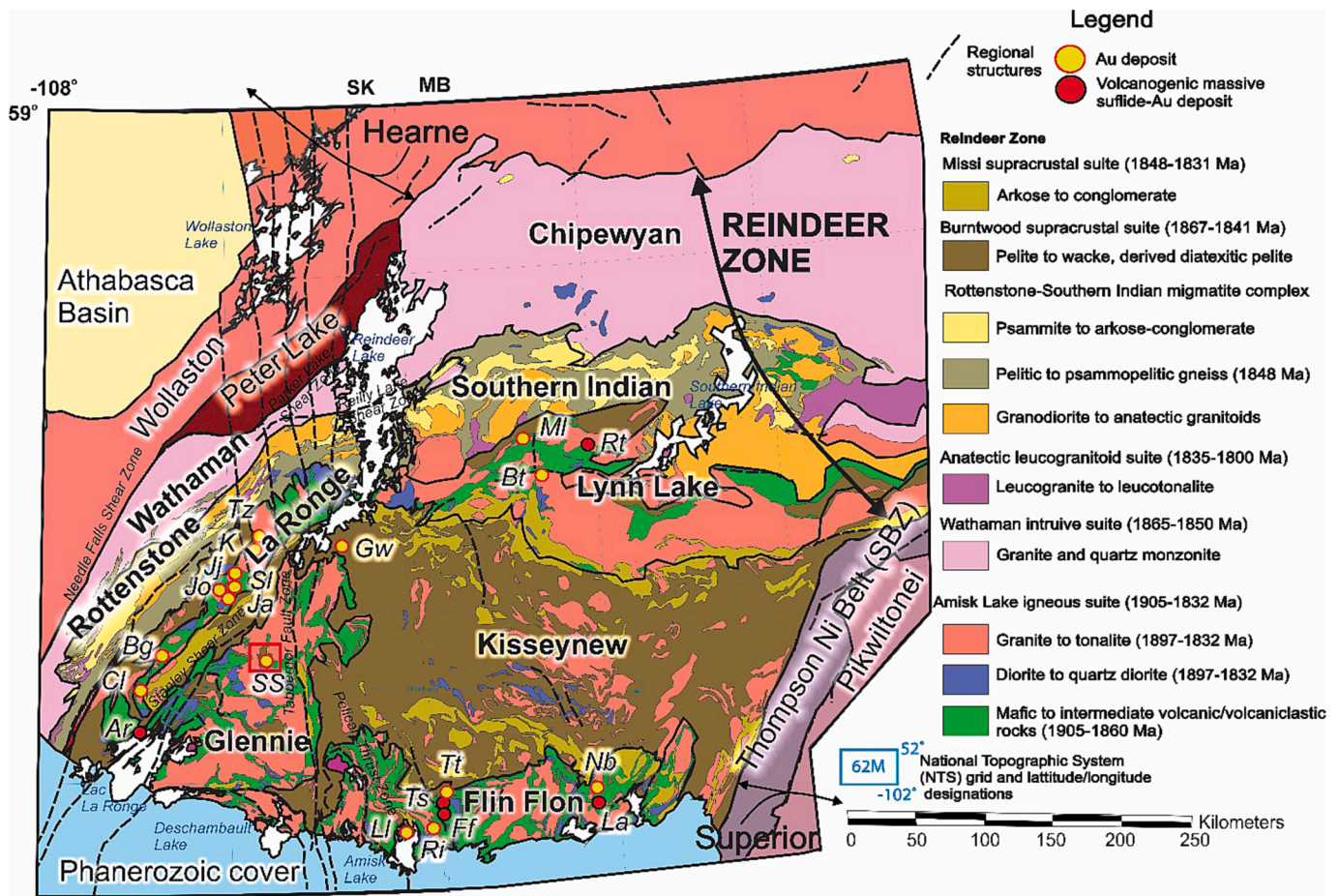


Fig. 1. Geological map showing the lithostructural subdivisions of the Precambrian rocks in Saskatchewan (SK) and Manitoba (MB), comprising the Hearne province (Wollaston, Peter Lake), Reindeer zone, Superior province (Pikwitonei, Thompson Ni Belt) and Athabasca Basin, below the younger Phanerozoic cover. Red box identifies study area shown in Fig. 2. The detailed geology and ages for domains within the Reindeer zone is based on Maxeiner and Kamber (2011) and Manitoba Geological Survey (2018). Lithological classifications in Manitoba are correlated to the lithology outlined in Maxeiner and Kamber (2011); SBZ: Superior boundary zone. The following are deposit annotations: Ar: Anglo-Rouyn; Bg: Bingo; Bt: Burnt Timber; Pf: Flin Flon; Gw: Greywacke; Jo: Jokay; K: Komis; La: Lalore; Ll: Laurel Lake; Ml: MacLellan; Nb: New Britannia; Ri: Rio/Bootleg; Rt: Ruttan; SS: Seabee, Santoy; Sl: Star Lake; Tt: Tartan Lake; Ts: Triple 7; Tz: Twin zone.

These deposits typically yield a Au-Te-Bi  $\pm$  W, Mo, Cu, Pb, Zn, As, Sn, Sb polymetallic signature, dependant on intrusion composition, oxidation state, and tectonic setting of formation (Sillitoe and Thompson, 1998). In contrast to the dominant occurrence of native gold in orogenic gold systems, intrusion-related systems typically yield invisible gold or micro-inclusions within disseminated sulfide minerals amongst fine-grained disseminated native gold (Sillitoe and Thompson, 1998, Ispolatov et al., 2008, Mériaud and Jébrak, 2017).

The protracted evolution of the Reindeer zone provides multiple geodynamic and tectonic settings in which various deposit types have formed (Corrigan et al., 2007). The La Ronge-Lynn Lake belt and Flin Flon domain, located to the west and east of the Glennie domain, respectively, hosts multiple orogenic gold deposits (Fig. 1; e.g., Ansdell and Kyser, 1992, Thomas and Heaman, 1994, Lawley et al., 2020). In these domains, orogenic gold deposits form within earlier ductile components of secondary and higher order shears that define the contact between, and cut into, upper greenschist to lower amphibolite grade mafic volcanic to siliciclastic rocks and adjacent tonalite to granite plutons (Van Schmus et al., 1987, Thomas and Heaman, 1994, Maxeiner and Kamber, 2011). These deposits include the well-known Maclellan, Star Lake, Jolu, Japsen, and Jojay deposits, as well as the Komis and Bingo deposits in the La Ronge-Lynn Lake belt (e.g., Thomas and Heaman, 1994, Hrdy and Kyser, 1995, Lafrance, 1999, 2000; Samson et al., 1999, Morelli and Maclachlan, 2012, Lawley et al., 2020). In the Flin Flon domain, these orogenic gold deposits include the Rio, and Tartan Lake deposits (e.g., Ansdell and Kyser, 1992, Fedorowich et al., 1995). By contrast, deposits that yield genetic associations between felsic intrusions and gold mineralization are known to occur within subduction-related arc tectonic environments (Sillitoe and Thompson, 1998). In the Reindeer zone, this association has been suggested for (i) the Bingo North and Bingo South showings in the La Ronge domain (e.g., Tourigny 2003a), with some researchers supporting a similar genetic relationship for the Komis deposit (e.g., Asbury, 1986); (ii) the Greywacke deposit in the Kisseynew domain (Morelli and Maclachlan, 2012); and (iii) multiple showings in the Brownell Lake Area of the Glennie domain (Delaney, 1992, Morelli and Maclachlan, 2012). In summary, the spatial relationships these orogenic-style deposits share with proximal intrusions have inspired debate regarding the nature of hydrothermal processes that governed their formation. Additionally, recent metallogenic studies have progressively identified a component of magmatic-hydrothermal input within orogenic terranes (e.g., Bucci et al., 2004, Mériaud and Jébrak, 2017, Mathieu, 2019). In terms of the Glennie domain, previous structural, fluid inclusion, and geochemical studies (e.g., Tourigny et al., 2004, McEwan, 2013, Wood, 2016) suggest orogenic-style mineralization at the Seabee and Santoy deposits. In contrast, a genetic link between gold mineralization and felsic dykes was also previously argued for the Seabee deposit (Helmstaedt, 1986, Tourigny 2003b, Tourigny et al., 2004). As such, this study provides further constraints towards the nature of structurally-controlled, intrusion-proximal gold mineralization from properties hosted within the Reindeer zone.

This study analyzes the mineral chemistry of samples from the Fisher property and Santoy Mine Complex from the Seabee Gold Operation, hosted within the Glennie domain of the Paleoproterozoic Trans-Hudson orogen (Fig. 1). At Santoy, auriferous quartz veins are hosted by the Santoy shear system, which (i) is interpreted to be a secondary splay off the crustal-scale Tabbornor fault system; (ii) are broadly developed along or proximal to contacts between intrusive rocks and mafic to intermediate volcanic to volcanoclastic rocks; and (iii) extend south through a structural corridor onto the Fisher property. Aside from the spatial relationship between shear-hosted mineralization and adjacent intrusions, the role these intrusions play and source of the hydrothermal fluid is still unknown. This study presents the lithological characteristics of host rocks and alteration assemblages, as well as the major and minor elemental variation, mineralogical trends, and geothermobarometric conditions of alteration minerals associated with sulfide-gold mineralization from the Fisher property and Santoy Mine Complex host rocks.

This data can facilitate the development of a metallogenic model and determine the relationship between hydrothermal processes in the Pine Lake greenstone belt, as well as Fisher, Santoy, and adjacent intrusions. Additionally, this data will constrain the timing of gold mineralization throughout the Seabee Gold Operation, relative to regional processes in the Glennie domain and the Reindeer zone of the Trans-Hudson orogen.

## 2. Regional geology

### 2.1. Reindeer zone of the Trans-Hudson orogen

The extent of the Paleoproterozoic Trans-Hudson orogenic belt in the provinces of Manitoba and Saskatchewan is typically separated into three main components, comprising (i) the internal Paleoproterozoic Reindeer zone; (ii) the Hearne margin to the west; and (iii) the Superior margin to the east (Fig. 1; Stauffer, 1984). The structurally complex Reindeer zone includes litho-structural subdivisions of juvenile inter-nides, from west to east being the Wathaman-Chipewyan, Rottenstone-Southern Indian, La Ronge-Lynn Lake domains, as well as the Flin Flon-Glennie Complex and Kisseynew domain (Fig. 1; Lewry et al., 1994, Corrigan et al., 2005). These domains are comprised of rocks generated from primitive to evolved volcanic arcs, inter-arcs, successor arcs, marginal sedimentary basins, and associated plutonism generated within the Manikewan Ocean between ca. 2.07–1.80 Ga (Stauffer, 1984, Hoffman, 1988, Ansdell, 2005, Corrigan et al., 2009).

The tectonic evolution of the Reindeer zone encompasses episodes of convergence as the Manikewan Ocean closed (Corrigan et al., 2005, 2009). The oldest rocks are associated with juvenile arc formation and *syn*-volcanic plutonism (Van Schmus et al., 1987, Chiarenzelli, 1989, Stern et al., 1995) during the initial closure of the Manikewan Ocean from ca. 1.92–1.88 Ga (Lewry and Collerson, 1990, Corrigan et al., 2005). Intra-oceanic accretion of these older arc rocks (regional D<sub>1</sub> deformation), formed the Flin Flon-Glennie complex ca. 1.87 Ga, comprising the Snow Lake arc assemblage, Amisk collage, Hanson Lake block, and the Glennie domain (Lewry et al., 1990, Lucas et al., 1996, Ashton, 1999). Continued west-dipping subduction under the eastern Hearne craton margin, led to accretion of the La Ronge-Lynn Lake arc and the generation of the Wathaman-Chipewyan batholith (ca. 1.865–1.855 Ga; Fumerton et al., 1984, Meyer et al., 1992, Corrigan et al., 2005, 2009) which were coeval with successor-arc and continental-arc plutonism in the Flin Flon-Glennie Complex (Bickford et al., 1987, Chiarenzelli, 1989). The Flin Flon-Glennie complex collided with the previously accreted La Ronge-Lynn Lake arc (Zwanzig, 2000, Corrigan et al., 2005), prior to subsequent rifting of the Flin Flon-Glennie complex (ca. 1.85–1.84 Ga) to form a back-arc basin, deposition of continental sediments (Ourum, Pine Lake, Missi, and Wapawekka groups), and post-successor arc magmatism (Ansdell et al., 1995, Corrigan et al., 2009). Additionally, subsequent (ca. 1.84–1.83 Ga) collision between the north-shifting Sask craton with the overriding Flin Flon-Glennie complex generated the Pelican thrust, a structural zone separating the Glennie domain and underlying Sask Craton (Ashton et al., 2005).

The final main episode (ca. 1.83–1.80 Ga) encompasses the collision between the Superior craton, Reindeer zone, and Hearne craton, resulting in the final closure of the Manikewan Ocean, late-arc intrusions and cessation of successor arc plutonism ca. 1.83–1.825 Ga, (Van Schmus et al., 1987, Ansdell, 2005, Corrigan et al., 2009), as well as widespread deformation (D<sub>2</sub>) and peak regional metamorphism (Lewry and Collerson, 1990). Late- to post-collisional deformation (D<sub>3</sub>) is present throughout the Reindeer zone (Lewry et al., 1990, Elliott, 1995, Wood, 2016), and includes the generation and reactivation of shear structures semi-coeval with orogenic gold mineralization throughout the Flin Flon, Glennie, and La Ronge domains (Fig. 1; Corrigan et al., 2007).

## 2.2. The Glennie domain

Occupying the western portion of the Flin Flon-Glennie complex, the Glennie domain is constrained by the northeast-trending Stanley shear zone in the west, Phanerozoic sedimentary cover in the south, as well as mylonites and overlying orthogneisses to the east, roughly defining the Kiskeynew boundary that extends south along the Hanson Lake Block contact (Fig. 1; Delaney and Cutler, 1992, Ashton, 1999). The Glennie domain generally comprises volcanic, arkosic, and pelitic/psammopelitic assemblages, occurring among plutonic rocks, and structurally overlying the Archean granitoids of the Sask craton (Delaney and Cutler, 1992). The Glennie domain is dominated by subordinate and elongate supracrustal belts which have undergone multi-phase deformation, and associated regional upper greenschist to lower amphibolite grade metamorphism, peaking at  $1810 \pm 10$  Ma (Durocher et al., 2001, Schneider et al., 2007). Specifically, the rocks in the Glennie domain were buried to temperatures and pressures around 500–650 °C and 2.5–7 kbar during  $D_2$  (Durocher, 1997) and 655–705 °C and 6.1–7.3 kbar during  $D_3$  (Durocher et al., 2001).

## 2.3. The Pine Lake greenstone belt

The supracrustal rocks of the Pine Lake greenstone belt in the northeastern section of the Glennie domain and hosting the Seabee Gold Operation, are divided into three assemblages (Fig. 2). The first being the older (ca. 1884–1870 Ma; Delaney and Cutler, 1992, Durocher et al., 2001, Witvoet, 2023) mafic to intermediate, volcanic to volcanoclastic rocks of Assemblage A (Fig. 2). The  $1879 \pm 1.3$  Ma (Witvoet, 2023) plutonic rocks of the multiphase Laonil Lake intrusive complex intrudes this assemblage to the west near the Seabee deposit, consisting of gabbro, diorite, minor lenses of granodiorite, and intermediate-felsic dykes (Chiarenzelli, 1989). Also intruding this assemblage is the  $1859 \pm 5$  Ma granodioritic Eyahpaise Lake pluton south of the Seabee mine (Van Schmus et al., 1987), the oldest  $1883.8 \pm 0.9$  Ma quartz gabbro from the multiphase Eisler intrusive suite to the southeast near Fisher (Witvoet, 2023), and the  $1874.6 \pm 1.9$  Ma tonalitic Lizard Lake pluton to the east near the Santoy deposits (Fig. 2; Wood, 2016). The second assemblage comprises younger (ca. 1840 Ma; Delaney and Cutler, 1992, McNicoll et al., 1992), unconformably overlying, felsic volcanic to volcanoclastic and sedimentary rocks of Assemblage B. The third assemblage constitutes a younger (inferred; ca. <1830 Ma), unconformably overlying, siliciclastic succession of the Porky Lake Group, occurring primarily within the core of the Ray Lake synform to the northwest (Fig. 2; Delaney and Cutler, 1992, McNicoll et al., 1992). The Assemblage A units are typically cut by the Santoy shear zone, a secondary shear structure that splays off a ductile component of the crustal-scale Tabernor system, with quartz veins and associated gold mineralization occurring within or adjacent to the secondary structures (Delaney and Cutler, 1992, Durocher et al., 1992, Wood, 2016). The boundary between Assemblage A and B rocks is characterized by a laterally extensive basal polymictic conglomerate unit of Assemblage B and is intercalated with a rhyolite near Porky Lake ( $1838 \pm 2$  Ma; McNicoll et al., 1992). These supracrustal units were subsequently cut by granodioritic plutons and pegmatite dykes, including the  $1807 \pm 7$  Ma anatectic Packman Lake pluton to the southwest of Santoy (Lewry et al., 1990, Wood, 2016).

Regionally,  $D_1$  deformation comprises overall north- to northwest-trending tight to isoclinal folds ( $F_1$ ) and associated composite, axial-planar schistosity ( $S_{0/1}$ ) from intra-oceanic accretion and southwest directed thrusting (Lewry et al., 1990). Subsequent ductile deformation ( $D_2$ ) ca. 1840–1800 Ma during Manikewan corridor closure generated (i) east–west-trending folds ( $F_2$ ); (ii) transposed regionally pervasive, axial-planar  $S_2$  foliation ( $S_{0/1/2}$ ); and (iii) ductile shear zones and domain-bounding high-strain zones (Lewry et al., 1990, McEwan, 2013, Wood, 2016). Late- to post-collisional  $D_3$  deformation (ca. 1800–1735 Ma) is defined by large, north-northwest-plunging folds, from west to

east being (i) the Ray Lake synform; (ii) the Carruthers Lake antiform; and (iii) the Carruthers Lake synform (Fig. 2; McEwan, 2013, Wood, 2016). Additionally, late- to post collisional  $D_3$  is defined by (i) north–south-trending transposed axial planar foliation ( $S_3$ ) as well as shear zone development and reactivation; (ii) Type 2 and 3 interference folds ( $F_{2-3}$ ); and (iii) transition of Tabernor shear movement from dextral-reverse oblique-slip (early- $D_3$ ) to terminal ductile  $D_3$  sinistral strike-slip (Elliott, 1995, Wood, 2016).  $D_4$  brittle deformation is regionally recognized as northeast-plunging type I interference folds ( $F_4$ ), generating regional dome-basin structures coeval with the post-collisional shortening between the Rae-Hearne and Superior cratons (Lewry, 1977, McEwan, 2013).

## 2.4. Mineralization at the Seabee Gold Operation

The host rocks that occupy the Seabee Gold Operation typically include sheared and altered Assemblage A and intrusive lithologies. Previous studies (e.g., McEwan, 2013, Wood, 2016, Srk Consulting, 2017, Onstad, 2021) indicate that the Fisher and Santoy properties yield comparative lithologies, mineralogy, and textures, and suggest that the lithology and structures at Santoy extends south through the structural corridor onto the Fisher property. Furthermore, these studies identified resemblance between the prominent  $S_3$  foliation, textures, characteristics, and mineralogy of Fisher and Santoy host rocks and confirm that deformation along the Santoy shear system likely was analogous in nature and occurred concurrently.

Characteristics of gold mineralization, however, vary throughout the Seabee Gold Operation, including the Seabee and Santoy deposits, as well as current exploration targets, such as the Fisher property (e.g., Durocher et al., 1992, Tourigny 2003a,b, Wood, 2016, Kenwood, 2017). Generally, mineralization at Seabee consists of shear-controlled (Laonil Lake shear system) auriferous quartz-tourmaline-carbonate veins that contain low grade (~7 g/t; Srk Consulting, 2017), free to sulfide-bound gold, hosted within the multiphase Laonil Lake intrusive complex adjacent to felsic dykes (Basnett, 1999, Tourigny 2003b, Tourigny et al., 2004). These characteristics change at Santoy, which comprises shear-hosted auriferous quartz-carbonate veins, yielding slightly higher-grade (~10 g/t; Srk Consulting, 2017) native to sulfide-bound gold within Assemblage A rocks adjacent to granodiorite intrusions (Durocher et al., 1992, McEwan, 2013). In general, however, gold mineralization at Santoy is spatially associated with secondary shear splays off the Tabernor system, specifically located along the Santoy shear zone, which roughly defines basalt-granodiorite contacts (Fig. 2; Delaney, 1986, Durocher et al., 1992). As such, the regionally pervasive east–west-trending  $S_2$  foliation is strongly transposed in shear-adjacent lithologies to north–south-trending  $S_3$  fabrics that parallel shear zone orientation. At the Santoy Mine Complex the ore bodies occur sub-parallel, dip 40° – 60° east, and plunge to the north, yielding distinct structurally-controlled mineralization concentrated within a dilatational jog along the Santoy shear system (Fig. 2). Although the relationship between mineralization and adjacent granodiorite to diorite-tonalite intrusions ( $1874.6 \pm 2.9$  Ma), genetically related to the  $1874.6 \pm 1.9$  Ma Lizard Lake pluton, was previously unknown at Santoy, multiple lines of evidence suggest a structural relationship and orogenic-style mineralization (Wood, 2016). Hydrothermal titanite from the gold-associated calc-silicate alteration assemblage was dated at  $1755 \pm 8$  Ma, which post-dates adjacent dykes, and eliminates a model proposing a syngenetic relationship between intrusions and gold mineralization (Wood, 2016). Furthermore, a pegmatite dyke ( $1736 \pm 1.9$  Ma) that crosscuts zone 8 mineralization records final stage  $D_3$  ductile deformation and provides a minimum age of gold mineralization (Wood, 2016). Additionally, the Packman Lake pluton is proposed to have acted as a buttress during  $D_3$  (minimum age of flexure  $1807 \pm 7$  Ma), causing a compressional jog within the Santoy shear zone (Gap; Fig. 2), increasing fracture density and potential for mineralization (Cox et al., 2001, Wood, 2016).

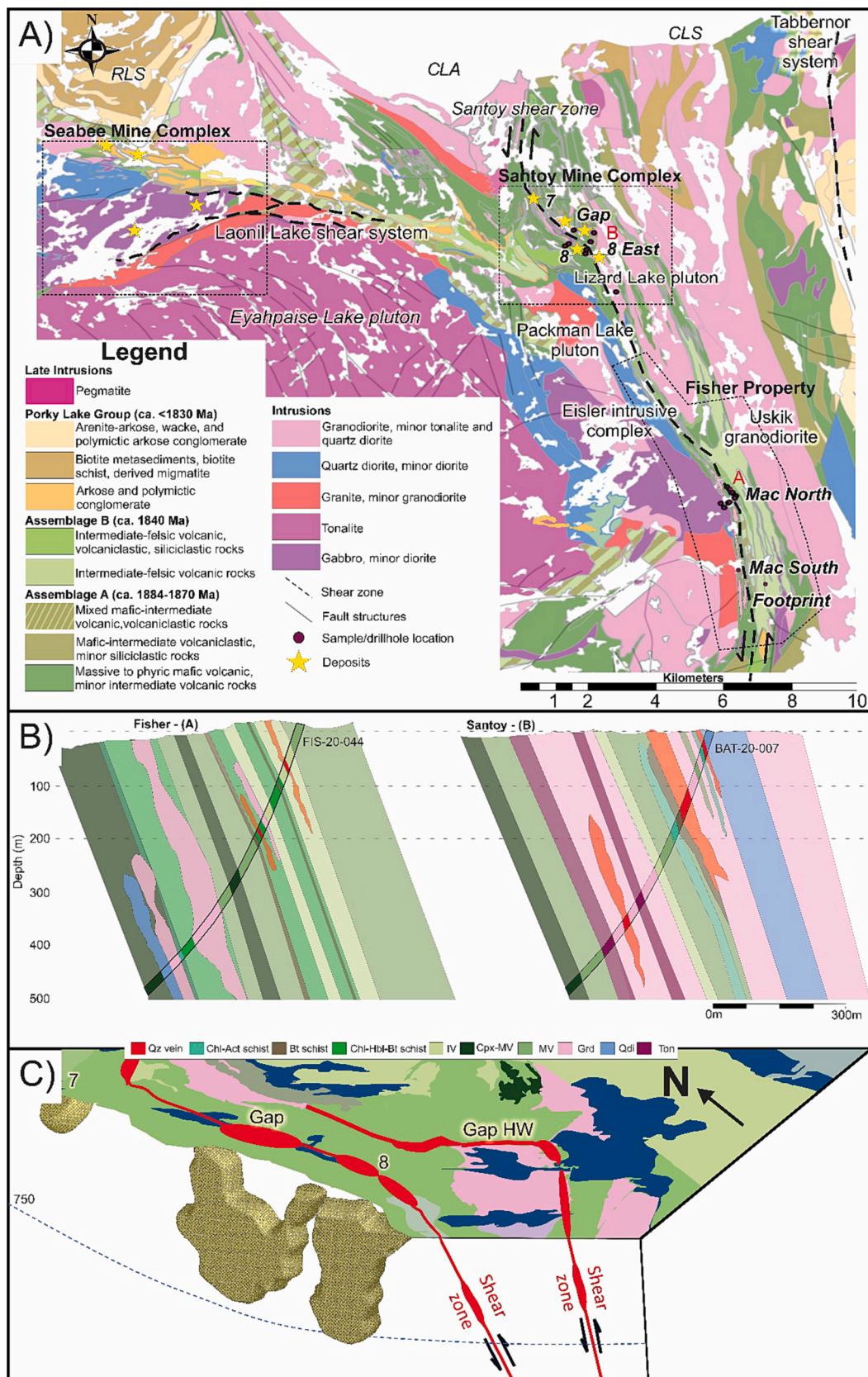


**Fig. 2.** (A) Geology of the Pine Lake greenstone belt of the area highlighted in Fig. 1 showing the Seabee Mine Complex, Santoy Mine Complex, and Fisher property, as well as important units and surrounding structures (modified from Delaney, 2016). RLS: Ray Lake synform; CLA: Carruthers Lake antiform; CLS: Carruthers Lake synform. (B) Cross-sections from red-highlighted points A (Fisher – Mac North) and B (Santoy – Gap). (C) Deposit model showing that gold deposits are contained within a releasing bend on the Santoy shear zone. The following are the labels for (B) and (C) IV: intermediate volcanic; Cpx-MV: clinopyroxene-phyric mafic volcanic; MV: mafic volcanic; Grd: granodiorite; Qdi: quartz-diorite; Ton: tonalite.

### 3. Materials and methods

A total of 46 samples (see Appendix A for sample details) were collected from two main locations along a 16 km trend of the Santoy shear zone, including the Santoy 7 and Santoy Gap deposits, as well as Fisher property. Targeted samples include supracrustal and intrusive rocks with variable alteration and mineralization. These samples were cut into 58 polished thin sections and analyzed by transmitted and reflected light petrography using a Nikon Eclipse E200 polarizing microscope to determine rock type. Additionally, an in-depth analysis of vein and vein-adjacent mineralogy supported the construction a paragenetic sequence and identification of hydrothermal phases associated with the degree of alteration or mineralization.

#### 3.1. Mineral prefixes

Subsequent mineral names utilize the Whitney and Evans (2010) nomenclature, with the prefix “meta-” removed from lithology names as all rocks in this have been subjected to metamorphism. Phases were identified within the unaltered to vein-adjacent alteration assemblages, where “WR-” denotes the unaltered and foliated wall rock mineral phase, and “H-” denotes the wide halo-shear alteration, which are in the unaltered and distal halo (~0.4–3 m wide) alteration assemblage, respectively. Additionally, “VA-” indicates mineral phases located in the proximal (10–40 cm wide) to vein-adjacent (3–30 cm wide) alteration assemblage, and “V-” denotes phases hosted within quartz veins.

#### 3.2. Electron probe microanalysis

Major and minor element compositions of sixteen samples consisting of alteration minerals and associated mineralization within Assemblage A and intrusive rocks were determined by a Cameca SX-100 electron microprobe housed at the Department of Earth Sciences, University of Manitoba, Canada. Operating conditions for silicate and apatite analyses include an accelerating potential of 15 kV, beam currents of 10–20 nA, beam sizes of 1–10 µm in diameter, and 20 s counting times on both peak and background. For sulfides and BiTe mineral phases, an accelerating potential of 25 kV, beam currents of 5–20 nA, a beam diameter of 1 µm, and counting times of 20 s on peak and background were used. X-ray intensities were standardized using natural standards in silicate, synthetic phosphates for REE in apatite, and synthetic and pure metals in sulfide and BiTe mineral phases. Pouchou and Pichoir (1984) matrix correction scheme was applied to all analyzed phases using an x-ray form factor, attenuation and scattering (FFAST) mass absorption coefficient table (Chantler, 2000). Oxygen was estimated using stoichiometry and all Fe was treated as FeO except for mineral phases that are known to have ferric iron such as biotite, amphibole, epidote, clinopyroxene, and feldspar. Mineral formula calculations were carried out with MS Excel spreadsheets downloaded from GabbroSoft (2011) and plotted using IoGas. Abnormally high analytical totals in BiTe mineral phases are attributed to micro-inclusions.

### 4. Results

#### 4.1. Representative lithologies

The Seabee Gold Operation encompasses the Santoy Mine Complex and Fisher property, hosted within the Paleoproterozoic rocks of the Glennie domain. The supracrustal rocks at the Santoy Mine Complex and Fisher are dominated by the various volcanic, volcanoclastic and sedimentary rocks (Fig. 2) of Assemblage A (ca. 1884–1870 Ga; Delaney and Cutler, 1992, Durocher et al., 2001, Witvoet, 2023), which generally strikes north-northwest and dips steeply at around 75–95° to the east (Fig. 2; Onstad, 2021). In this area, Assemblage A rocks typically occur between the Packman Lake pluton and Eisler intrusive complex to the west of Santoy and Fisher, respectively, with the Uskik granodiorite in

the east (Fig. 2). Various granodiorite to tonalite intrusions cut Assemblage A rocks and share a similar north-northwest strike with the surrounding supracrustal rocks.

Samples in this section are of least-altered metamorphosed host rocks to provide context for the following sections. Mineral abundances for the following lithologies are shown in Table 1. Because this paper primarily addresses altered samples, lithologies present on the property that do not correlate with an unaltered equivalent are excluded. The lithologies are consistent extending from the Santoy Mine Complex through to the Fisher property. As these units extend south towards the tighter section of the shear corridor at Fisher, a noticeable grain size reduction is observed and is specifically apparent in the intrusive units. Additionally, the units become deformed, foliated, sheared, and altered proximal to the Santoy shear system and associated mineralization.

#### 4.1.1. Assemblage A lithologies

**4.1.1.1. Mafic volcanic unit.** One of the thickest units (~1 km) that extends from the Santoy Mine Complex to the Fisher property is the mafic volcanic unit (Figs. 2 and 3A), which is the dominant host rock of gold mineralization. This unit typically occurs as fine- to medium-grained, but often yields concordant gradational contacts with clinopyroxene-phyric mafic volcanic rock and gradational to sharp concordant contacts with minor units of intermediate volcanic rock. The mafic volcanic unit is dark grey/black/green in colour and characterized by hornblende porphyroblasts associated with biotite and chlorite within a quartz and plagioclase groundmass. Also present are accessory sulfide minerals and apatite, epidote, and titanite. The clinopyroxene-phyric mafic volcanic rock (Fig. 3B) is identifiable by the mm-scale relict primary clinopyroxene phenocrysts and hornblende porphyroblasts associated with chlorite and biotite and hosted within a fine-grained groundmass of plagioclase and minor quartz. The main fabric (S<sub>2</sub>) has been transposed to S<sub>3</sub> from extensive shearing and is defined primarily by biotite, chlorite, and hornblende.

**4.1.1.2. Intermediate volcanic unit.** The intermediate volcanic unit (~200 m thick; Onstad, 2021) is typically fine-grained, medium grey, and primarily in contact with the mafic volcanic unit (Figs. 2 and 3C). The intermediate volcanic rocks have distinguishable blotchy elongated blebs of albite-quartz ± K-feldspar-epidote alteration that are ~2 cm wide and moderately- to widely-spaced. Generally, this unit comprises hornblende porphyroblasts, biotite, chlorite, and accessory fine- to medium-grained apatite, epidote, and titanite within a quartz and plagioclase groundmass. The S<sub>3</sub> fabric is primarily defined by biotite, chlorite, and hornblende.

**4.1.1.3. Volcanoclastic unit.** Volcanoclastic equivalents of the above units are also present in variable thicknesses that extend from Santoy to Fisher. This unit is primarily characterized based on macroscopic features, including bedding and clasts. The volcanoclastic lithology, however, becomes indistinguishable with increased proximity to the Santoy shear system and resulting shearing, alteration, and mineralization. These volcanoclastic rocks are primarily dacitic to andesitic in composition and occasionally present as tuffs.

#### 4.1.2. Intrusive lithologies

**4.1.2.1. Granodiorite.** The intrusive units (Figs. 2 and 3D–F) typically intrude Assemblage A, where granodiorite observed near the Santoy shear system at the surface and at depth (Figs. 3E and 2). This granodiorite unit comprises subequal amounts of equigranular and coarse-grained sericitized plagioclase, alkali feldspar, and quartz phenocrysts, as well as minor muscovite and biotite, which roughly defines a weak foliation. Also present are accessory fine- to medium-grained disseminated sulfide minerals, magnetite, ilmenite, and titanite, apatite,

**Table 1**  
Mineralogical composition (%) of unaltered lithofacies, sheared equivalents, and associated alteration assemblages. Alteration minerals section comprises numerous phases associated with each lithofacies or alteration assemblage.

	Unaltered						Altered											
	Assemblage A			Intrusive			Assemblage A							Intrusive				
	MV	Cpx-MV	IV	Grd	Qz-Di	Ton	Hbl-Bt meta-basalt	Chl-Hbl-Bt schist	Chl-Act schist	Bt schist	Distal halo	Proximal	Vein-adjacent	Grd-Ton	Distal halo	Proximal	Vein-adjacent	
Pre-alteration minerals	Cpx	–	35–45	–	–	–	–	–	–	–	–	–	–	–	–	–	–	–
	Am	25–50	20–25	15–20	–	<5	–	10–25	10–15	10	10	<5–5	<5	–	–	–	–	–
	Bt	5–15	5–10	5–15	5–10	5–10	5–20	15–20	–	10–15	<5–5	<5	–	5–10	<5–5	–	–	–
	Chl	5–15	5–10	5–15	<5	<5	–	5–10	10–15	5	<5–5	<5	–	<5	<5	–	–	–
	Ms	–	–	–	5–10	5–10	–	–	–	–	–	–	–	–	–	–	–	–
	Grt	Tr-<5	Tr-<5	–	–	–	–	tr	–	–	–	tr	–	–	–	–	–	–
	Kfs	–	–	–	10–25	10	5–10	–	–	–	–	–	–	–	–	–	–	–
	Pl	15–20	20–30	10–25	30–40	60–65	40–50	10–15	5–10	5–10	5–10	5–10	<5–5	–	30–65	10–20	10–15	<5–5
	Qz	–	–	–	20–30	15–20	30–40	–	–	–	–	–	–	–	15–40	5–20	5–10	<5–5
	Ap	<5	<5	<5	tr	tr	tr	–	tr	–	–	–	–	tr	tr	–	–	–
	Ep	<5	<5	<5	tr	tr	tr	–	tr	5–10	<5	–	–	–	tr-5	tr	–	–
	Ttn	<5	<5	<5	<5	<5	<5	–	tr	tr	<5	–	–	<5	tr	<5	–	–
Alteration minerals	Qz	5–15	5–10	20–30	–	–	–	10–15	10–15	5	5–10	5–10	5–10	5–10	<5	5–10	5–10	5–10
	Ser	5	5	5	5–10	5–10	5–10	10	10–15	10–15	10–15	10–15	10–15	5–10	5–10	10–15	15–30	20–35
	Bt	<5	<5	–	<5	–	–	5–10	5–10	<5–5	20–30	15–20	10–15	<5–5	<5	5–15	5–15	10–25
	Chl	<5	<5	–	<5	–	–	5–10	5–10	20–25	5–10	10–15	10–15	5–10	<5	5–15	5–10	10–20
	Act	–	–	–	–	–	–	<5–5	5–10	20–25	<5	5–10	10–15	5–10	–	–	<5–5	<5–5
	Di	–	–	–	–	–	–	–	tr	tr	–	<5	<5–5	15–20	–	tr	tr	tr
	Czo	–	–	<5	–	–	–	tr	tr	tr	5–10	5–10	5–10	5–10	–	<5–5	<5	<5–10
	Ab	–	–	–	–	–	–	5	5	5	5	10–15	5–10	15–20	<5	<5	5–10	5–15
	Kfs	–	–	5	–	–	–	–	tr	tr	tr	tr	<5–5	10–15	<5–5	5–10	5–10	5–15
	Ttn	–	–	–	–	–	–	tr	<5	<5	<5–5	5	<5–5	5–10	<5	5	5	5
	Cal	–	–	–	–	–	–	–	<5	<5	–	<5	<5	<5–5	–	<5	<5	<5–5
	Ap	–	–	–	–	–	–	tr	<5	<5	<5	<5–5	<5–5	<5–10	–	–	<5	<5–5
	Py	tr	tr	tr	tr	tr	tr	<5	<5	<5	<5	<5–5	<5–5	<5–5	tr	<5	<5	<5–5
	Po	tr	tr	tr	Tr	Tr	Tr	<5	<5	<5	<5	<5	<5–5	<5–5	Tr	tr	<5	<5
	Cpy	Tr	tr	Tr	<5	<5	<5	<5	<5	<5	tr	<5	<5	<5	<5	<5	<5	<5–5
	Sp	Tr	Tr	Tr	Tr	Tr	Tr	tr	tr	tr	tr	<5	<5	<5	Tr	<5	<5	tr-5
	Apy	–	–	–	–	–	–	–	–	–	–	–	tr	tr	–	–	–	tr
	Tel	–	–	–	–	–	–	–	–	–	–	–	tr	tr	–	–	–	tr
	Au	–	–	–	–	–	–	–	–	–	–	–	tr	tr	–	–	–	tr
	Sch	–	–	–	–	–	–	–	–	–	–	–	–	tr	–	–	–	–
	Mt	Tr	Tr	Tr	<5	<5	<5	Tr	tr	tr	tr	<5	<5	tr	<5	<5	<5–5	<5–5
	Ilm	<5–5	<5–5	<5–5	<5–5	<5–5	<5–5	<5–5	<5–5	<5–5	5	5	<5	tr	<5–5	<5	<5	<5
	Hm	Tr	–	Tr	Tr	Tr	Tr	Tr	tr	tr	–	tr	tr	tr	Tr	<5–5	<5–5	<5
	Gn	–	–	–	Tr	Tr	Tr	–	tr	–	tr	tr	tr	Tr	<5	tr-<5	tr-5	tr-5
	Mo	–	–	–	–	–	–	–	–	–	–	–	tr	tr	–	–	–	tr

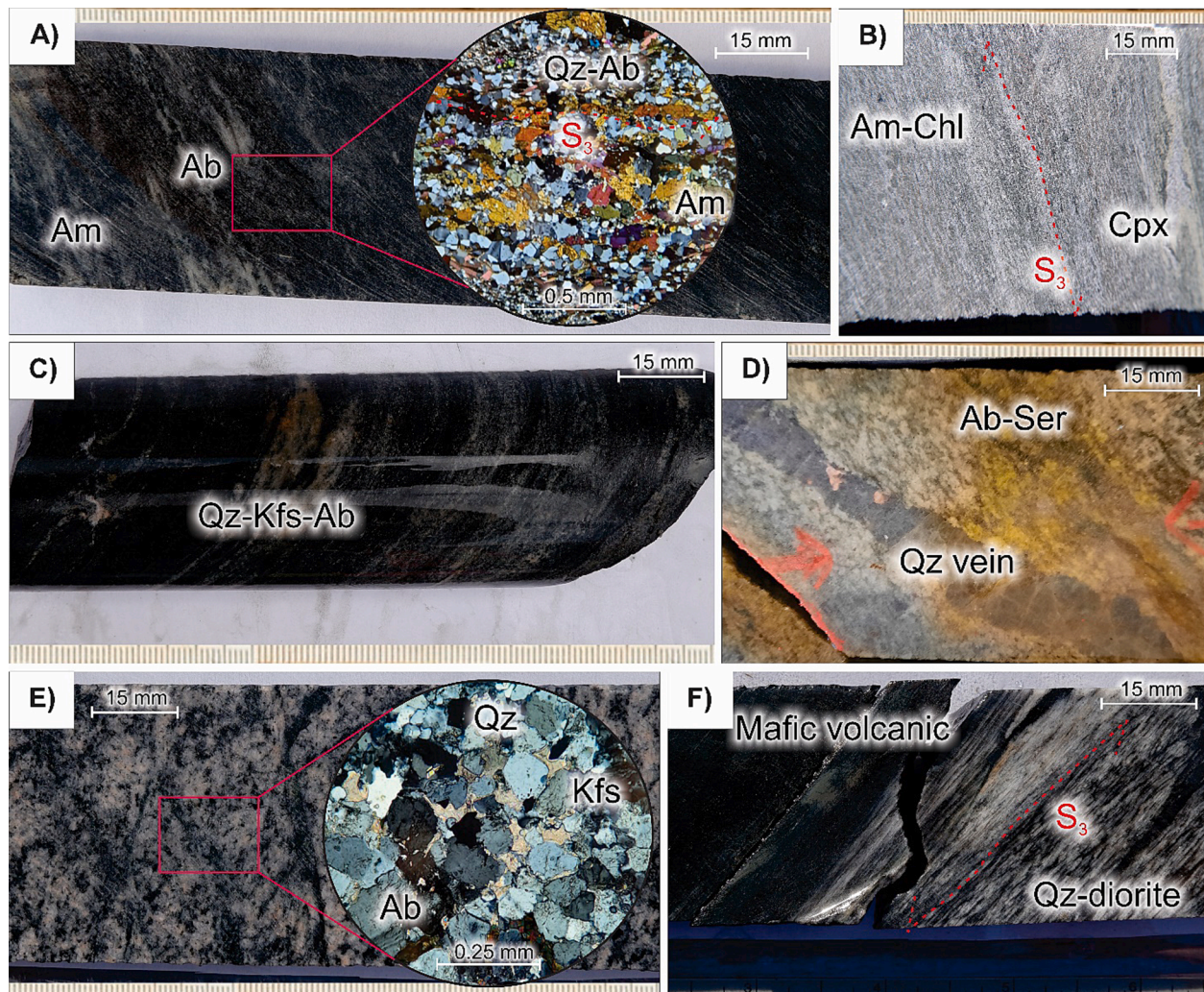


**Fig. 3.** Representative lithofacies from the Fisher and Santoy property. (A) Mafic volcanic with minor albite alteration. (B) Clinopyroxene-phyric mafic volcanic with chlorite and amphibole foliated around sub-mm-scale clinopyroxene. (C) Intermediate volcanic with cm-scale, blebby, K-feldspar-albite alteration. (D) Tonalite with albite-epidote alteration cut by thin quartz vein. (E) Medium-grained granodiorite with weak foliation. (F) Albitized contact between mafic volcanic and moderately foliated quartz diorite.

chlorite, and epidote. In comparison to the Santoy Mine Complex, this unit becomes more fine-grained at the Fisher property, which encompasses the narrow section of the shear corridor.

**4.1.2.2. Quartz-diorite and tonalite.** Also intruding Assemblage A, is the quartz-diorite unit which occurs in close proximity to granodiorite rocks and the Santoy shear system at depth (Fig. 2), and at the surface. This unit is characterized by a distinct speckled white-black appearance, however, is also occasionally present with secondary intermittent K-feldspar alteration and is similar in appearance to the granodiorite unit (Fig. 3F). The quartz-diorite unit comprises equigranular quartz, sericitized plagioclase, and alkali feldspar phenocrysts, and minor weakly foliated muscovite and biotite. Also present are medium-grained hornblende porphyroblasts, accessory disseminated sulfide minerals, magnetite, ilmenite, and fine- to medium-grained titanite, apatite, epidote, and chlorite. At Santoy, there is a noticeable decrease in quartz diorite units with an increase in tonalitic intrusions (Figs. 2 and 3D), comprising coarse-grained, equigranular quartz and sericitized plagioclase, and alkali feldspar phenocrysts, and similar minor and accessory mineralogy.

## 4.2. Altered lithologies

### 4.2.1. Sheared-altered assemblage A equivalent lithologies

The Fisher and Santoy lithologies become more strained and altered proximal to the Santoy shear system and associated mineralization. Generally, the lithologies are consistent between the Santoy Mine Complex and the Fisher property, comprising sheared intrusive rocks and Assemblage A equivalents which range from hornblende-biotite meta-basalt to chlorite-actinolite schist (Figs. 2 and 4A-E). The observed alteration assemblages (Fig. 5A-H) generally comprise a relatively wide (~0.4–3 m) distal biotite-sericite ± albite-titanite-clinozoisite halo assemblage, transitioning to a thin (~3–30 cm) quartz-carbonate vein adjacent assemblage, comprising coarse-grained diopside-albite-K-feldspar ± titanite-apatite-actinolite. Mineral abundances for the following lithologies and alteration assemblages are shown in Table 1.

**4.2.1.1. Hornblende-biotite meta-basalt.** The hornblende-biotite meta-basalt is present most distal to the Santoy shear system. Similarly, this sample is dark grey to black in colour and characterized by variable hornblende porphyroblasts and biotite within a subequal quartz and plagioclase groundmass (Fig. 4A). The samples also comprise minor sulfide minerals and accessory apatite, clinozoisite, and titanite.

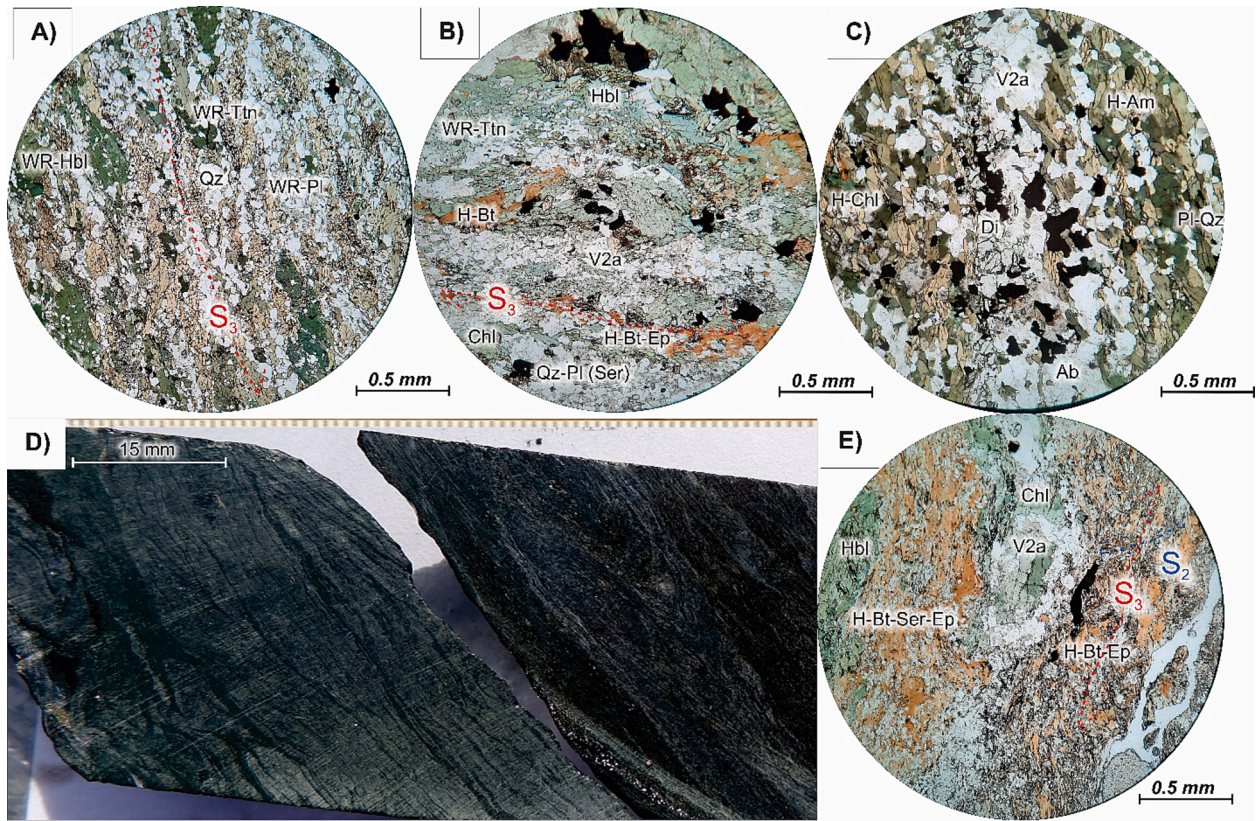


**Fig. 4.** Photomicrographs and hand sample images of sheared-altered Assemblage A lithologies. (A) Hornblende-biotite meta-basalt (20DBF-23). (B) Chlorite-hornblende-biotite schist cut by thin  $V_{2a}$  quartz vein (20DBF-16A). (C) Chlorite-actinolite schist cut by thin  $V_{2a}$  quartz vein with moderate vein-adjacent Di-Ab alteration (21DBS-10). (D) Chlorite-actinolite schist from FIS-20-057. (E) Bt-schist cut by  $V_{2a}$  quartz vein with minor-moderate chlorite alteration (20DBF-15).

Secondary variably intense chlorite alteration is apparent replacing biotite and hornblende, and moderate-strong sericite alteration is present as a fine-grained alteration on feldspar grains throughout the samples (Fig. 5A, E). Occasionally, these samples are cut by thin (mm-scale) biotite-sericite- to chlorite-dominated shear and alteration bands, similar in composition to the schists mentioned below, that often host thin (mm-scale) quartz  $\pm$  albite-sulfide veins (Fig. 5B).

**4.2.1.2. Chlorite-hornblende-biotite schist.** One of the most common sheared units is the chlorite-hornblende-biotite schist (Figs. 2 and 4B). This unit is dark brown/green/grey in colour and characterized by variable, fine-grained, strongly foliated chlorite, hornblende, biotite, and trace garnet porphyroblasts within a finer-grained matrix of moderate to strongly sericitized plagioclase, quartz, and biotite. Commonly, thin ( $\sim 0.12$ – $0.5$  mm) quartz-albite  $\pm$  carbonate-sulfide veins and thicker (cm- to m-scale) recrystallized quartz-sulfide  $\pm$  carbonate veins cut the wall rock concordant to foliation (Fig. 5C, G).

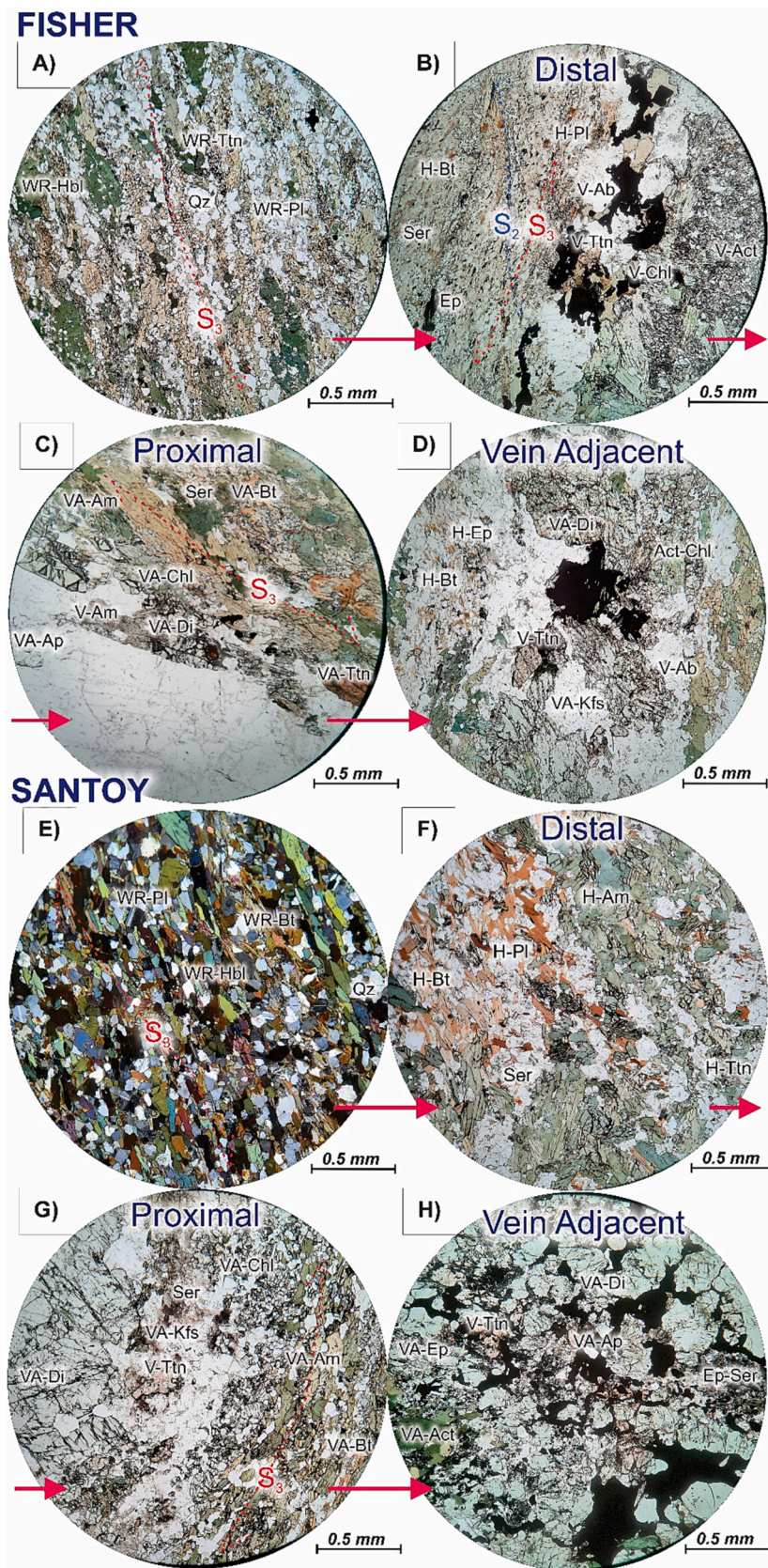
**4.2.1.3. Chlorite-actinolite schist.** The chlorite-actinolite schist (Figs. 2 and 4C, D) is observed in sharp contact with sheared chlorite-hornblende-biotite schist and biotite schist. This unit is typically dark green in colour and dominated by strongly foliated and crenulated chlorite and actinolite occurring amongst minor epidote within a sub-equal groundmass of sericitized plagioclase and quartz (Fig. 4C). Similarly, this unit is occasionally cut by thin (mm-scale) biotite-chlorite-dominated alteration bands, thin (0.12–0.3 mm) quartz-albite  $\pm$  sulfide-diopside veins, and less so by 1–30 cm recrystallized quartz  $\pm$  sulfide veins.

**4.2.1.4. Biotite schist.** The intensely sheared and foliated biotite-schist (Figs. 2 and 4E) primarily yields a gradational contact with less

sheared Assemblage A units and chlorite-hornblende-biotite schist. This unit is dark grey/brown in colour and dominated by fine-grained, strongly foliated and crenulated biotite associated with chlorite and foliated around minor hornblende porphyroblasts within a fine-grained groundmass of strongly sericitized plagioclase and quartz. Notably, the biotite schist present at the Santoy Mine Complex is coarser grained ( $\sim 0.5$ – $1.25$  mm) in comparison to that present at the Fisher property ( $\sim 0.12$ – $0.5$  mm). This unit is commonly cut by thin ( $\sim 0.12$ – $0.6$  mm) quartz-albite  $\pm$  carbonate-sulfide-diopside veins and large (cm- to m-scale), recrystallized quartz  $\pm$  sulfide-diopside veins concordant to foliation.

**4.2.1.5. Distal and proximal alteration assemblages.** The distal halo (0.4–3 m) alteration assemblage to these quartz veins and sheared segments is dominated by moderate to strong secondary biotite-chlorite-actinolite which is foliated around and overprints sericitized albite, medium-grained clinzoisite, fine-grained euhedral apatite, fine-grained anhedral disseminated titanite with ilmenite cores (Fig. 5B, F), and trace fine-grained diopside (Fig. 5B). Locally within this assemblage there is intense replacement of biotite with chlorite, commonly occurring adjacent to variably intense sulfide mineralization (Fig. 4E) or quartz veins. Minor foliation parallel, replacement-style pyrite-pyrrhotite-chalcocopyrite, disseminated fine-grained ilmenite, and trace magnetite occurs variably throughout this assemblage (Fig. 5B, F) amongst fine-grained, disseminated ilmenite and minor medium-grained sphalerite.

Proximal to these quartz veins (10–40 cm wide), mineralogy is dominated by fine- to medium-grained biotite-chlorite-actinolite alteration that defines C-S fabrics and is foliated around medium-grained clinzoisite, medium-grained sericitized albite, and fine- to medium-grained subhedral titanite, locally overprinted by medium-grained



(caption on next page)

**Fig. 5.** Photomicrographs showing progressive alteration from unaltered to vein-adjacent in Fisher (top) and Santoy (bottom) samples. (A) Hbl-porphyroblastic meta basalt (20DBF-23). (B) Distal Ser-Bt-Ep  $\pm$  Ab-Ttn halo alteration associated with V<sub>2a</sub> vein and vein-hosted Py<sub>2a</sub>-Chl-Act within a Chl-Hbl-Bt schist (20DBF-2A). (C) Proximal Ser-Bt-Chl-Am-Ttn-Ab-Cal  $\pm$  Ap-Ep-Di and vein-adjacent Di-Ttn-Kfs-Ap-Act alteration associated with V<sub>2b</sub> vein within a Chl-Hbl-Bt schist (20DBF-19). (D) V<sub>2a</sub> vein associated with vein-adjacent Di-Kfs-Ab-Act-Ttn  $\pm$  Ap alteration and Py with proximal Ser-Bt-Chl-Am-Ttn-Ep alteration within a Chl-Act schist (20DBF-13). (E) Lesser-altered segment of a meta-basalt with Hbl porphyroblasts within a fine-grained Qz and sericitized Pl groundmass (21DBS-10). (F) Bt-Ser-Ab-Ttn  $\pm$  Ep halo alteration distal to V<sub>2b</sub> vein within a Chl-Bt-Hbl Schist (21DBS-11). (G) Proximal Am-Ser-Chl-Bt-Ttn-Ab-Ep  $\pm$  Ap-Cal-Di and vein adjacent Di-Ttn-Kfs-Chl-Act alteration associated with V<sub>2a</sub> vein within a Bt-Hbl schist (21DBS-12). (H) Coarse grained Di-Act-Ttn-Kfs-Ap  $\pm$  Ab alteration within fine-grained Ep-Ser. Associated with Au-Po mineralization adjacent to V<sub>2b</sub> vein within a Chl-Ep-Hbl schist (SAN7-06).

acicular actinolite and fine-grained diopside (Fig. 5C, G). Pyrite-pyrrhotite  $\pm$  chalcopyrite-magnetite-sphalerite mineralization commonly forms replacement-style or fills fractures within this assemblage. Additionally, an increase in biotite-chlorite alteration occurs adjacent to sulfide minerals, which yield local associations with gold-telluride mineralization.

**4.2.1.6. Vein-adjacent alteration assemblage.** Overprinting the proximal alteration assemblage is a directly vein- and shear-adjacent (3–30 cm wide) calc-silicate alteration assemblage (Fig. 5D, H). Although the modal mineral percentage of this alteration assemblage varies, it generally includes coarse-grained albite and diopside, K-feldspar alteration, and variable titanite, apatite, and actinolite. Within this assemblage, the calc-silicate alteration occurs within a groundmass of primarily fine-grained sericite and clinozoisite. Typically, this alteration assemblage is boudinaged, with quartz and fine-grained pyrite-pyrrhotite mineralization present within the boudin necks. Although dominant pyrite-pyrrhotite mineralization is associated with this assemblage, regularly forming within fractures of more competent diopside grains and associated with gold and bismuth telluride mineralization (Fig. 5H), replacement-style pyrite-pyrrhotite often replaces actinolite and diopside and is cut by chalcopyrite. In areas with intense gold mineralization, tetradymite often forms around tellurobismuthite and/or around gold grains. In some samples, minor to trace scheelite, galena, hematite, molybdenite, arsenopyrite and more commonly medium-grained magnetite is present in this assemblage. In contrast, the Santoy samples show higher concentrations of pyrrhotite than pyrite associated with gold mineralization, where pyrite is replaced by pyrrhotite. Additionally, euhedral titanite sphenoids and anhedral apatite in this assemblage is much coarser-grained, both of which are associated with coarse-grained, anhedral K-feldspar and albite (Fig. 5H).

**4.2.1.7. Relative timing of alteration and relationship between properties.** Collectively, the distal halo and proximal alteration assemblages share similar characteristics between the Fisher property and Santoy Mine Complex. These alteration assemblages are concordant to foliation and generally gradational based on proximity to quartz veins and sheared segments which acted as fluid pathways. The semi-concordant orientation of quartz veins and associated alteration with dominant S<sub>3</sub> foliation present in samples from shearing suggests formation coeval with *syn*-late-D<sub>3</sub> deformation. Additionally, these alteration assemblages are also associated with foliation parallel, fracture-filling and replacement-style pyrite-pyrrhotite mineralization which coexists with gold mineralization. As such, the distal halo and proximal alteration assemblages and associated sulfide-gold mineralization represents the onset of main-stage gold mineralization during *syn*-late-D<sub>3</sub> deformation.

Characteristics of the vein adjacent calc-silicate alteration assemblage associated with pyrite-pyrrhotite  $\pm$  gold mineralization are also consistent between the Fisher property and Santoy Mine Complex. The overprinting relationship that the vein-adjacent alteration assemblage yields with the distal halo and proximal assemblages in conjunction with the semi-concordant orientation to strong S<sub>3</sub> foliation, suggests development during *syn*-late-D<sub>3</sub> deformation. It is important to note that due to continued D<sub>3</sub> deformation and the cyclical nature of structurally hosted mineralization, the distal to vein-adjacent alteration assemblages are likely semi-coeval and a product of multiple fluid pulses during the

same relative hydrothermal event. Although the calc-silicate alteration assemblage shares similar formation conditions and relative timing with the distal halo and proximal alteration assemblages, the overprinting relationship implies the subsequent generation of the vein-adjacent assemblage and associated mineralization during late continuous D<sub>3</sub> deformation. As a result of the continuous D<sub>3</sub> deformation event, the competent calc-silicate alteration assemblage became boudinaged and fractured, forming low pressure zones, in which sulfide-gold mineralization preferentially precipitated as well as remobilized during late-D<sub>3</sub>. These features are consistent between the Fisher property and Santoy Mine Complex samples and, as such, represent the cyclical nature of main-stage gold mineralization during multiple fluid injections during *syn*-late and late, ongoing D<sub>3</sub> deformation.

#### 4.2.2. Sheared-altered intrusive lithologies

**4.2.2.1. Sheared-altered granodiorite to tonalite.** The sheared intrusive units generally share similar mineralogy to their unaltered equivalents, however, the sheared lithologies portray moderate to intense grain-size reduction (Fig. 6C–F). Typically, these units yield sharp contacts or occur as rafts within adjacent sheared Assemblage A units and large (cm- to m-scale) recrystallized quartz  $\pm$  sulfide veins (Figs. 2 and 6A). Mineral abundances for the following lithologies and alteration assemblages are shown in Table 1. Distal to quartz veins and shear zones, halo alteration comprises intense sericitization of feldspars, associated with muscovite, fine-grained biotite, and chlorite of which strongly defines foliation and weak C-S fabrics. Within this assemblage disseminated, fine-grained titanite, clinozoisite, calcite, magnetite, ilmenite, hematite, and trace diopside is present (Fig. 6C, E). Sulfide mineralization occurs as fine- to medium-grained, foliation parallel, inclusion-rich, porous pyrite-chalcopyrite  $\pm$  magnetite and minor pyrrhotite (Fig. 6F). Proximal to quartz veins (10–40 cm wide), moderate to intense sericitization is present, associated with overprinting, fine- to medium-grained biotite-chlorite alteration. Late, overprinting K-feldspar-hematite alteration is also present and pervasively occurs over intermittent m-scale intervals (Fig. 6B).

**4.2.2.2. Vein-adjacent alteration assemblage.** The alteration assemblage directly adjacent to the veins and sheared intervals, overprints this vein- and shear-proximal mineralogy. This vein-adjacent assemblage comprises biotite, chlorite, intense sericitization, and minor muscovite, titanite, epidote, apatite, and trace diopside (Fig. 6D, F). Within this assemblage, fine-grained biotite and chlorite alteration overprint adjacent mineralogy and is associated with fine- to medium-grained sub-euhedral titanite and medium-grained, anhedral apatite (Fig. 6D). Sulfide minerals are dominated by medium-grained, porous inclusion rich pyrite-chalcopyrite and minor pyrrhotite mineralization. Within this assemblage medium-grained magnetite, sphalerite, and minor galena also occur adjacent to large, recrystallized quartz veins (12E). In these veins, similar mineralogy is observed with a local increase in magnetite-sphalerite  $\pm$  galena mineralization associated with mainly pyrite-chalcopyrite  $\pm$  pyrrhotite and potential gold mineralization (Fig. 7).

**4.2.2.3. Relative timing of alteration and relationship between properties.** Comparably, characteristics of the distal halo and proximal alteration assemblages in intrusive rocks are consistent between the Fisher

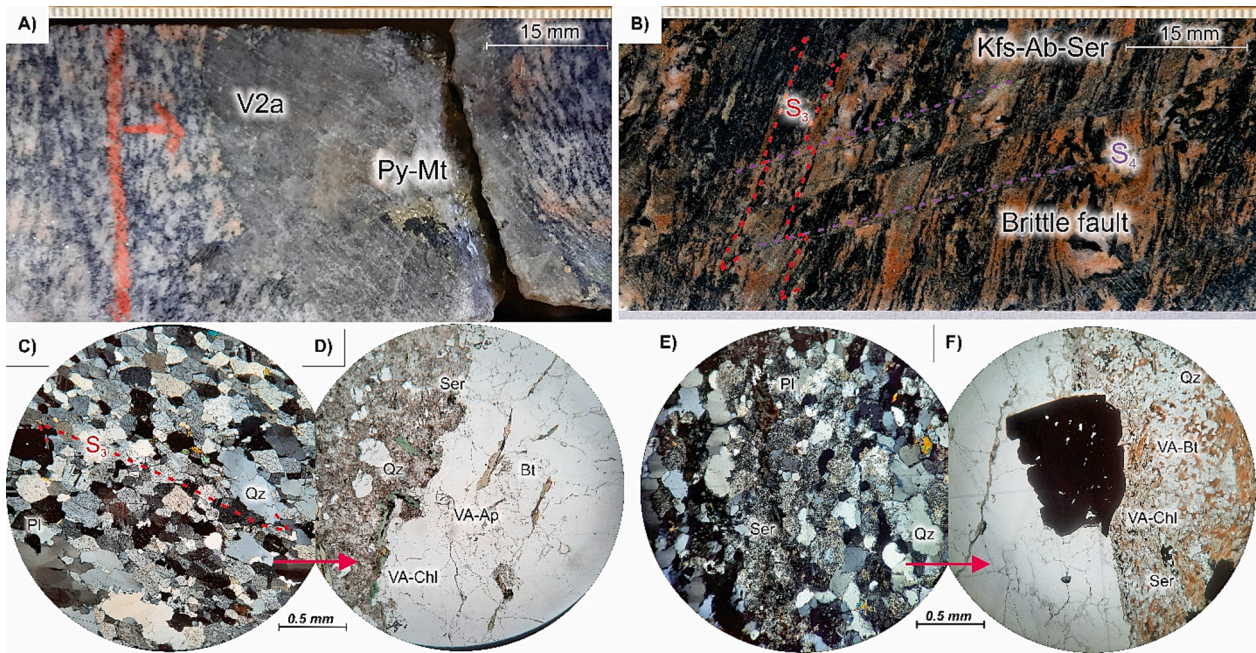


**Fig. 6.** Altered granodiorite with moderate Ser-Kfs-Ab alteration adjacent to  $V_{2a}$  vein, hosting Py-Mt-Cpy mineralization from Santoy Gap HW (21DBS-01). (B) Altered and sheared granodiorite with moderate Ser-Chl-Ep alteration cut by late, brittle,  $D_4$  faults that offset ductile  $D_3$  foliation (from FIS-20-057). (C) Coarse-grained tonalite defined by  $Pl > Qz$  and minor alkali feldspar phenocrysts with minor Ser alteration throughout sample (21DBS-05). (D) Medium-grained tonalite with intense Ser and minor to moderate Bt-Chl alteration adjacent to  $V_{2b}$  vein (21DBS-02). (E) Coarse-grained granodiorite defined by subequal Qz-Pl and minor alkali feldspar phenocrysts with moderate Bt-Ser alteration throughout sample (20DBF-11). (F) Recrystallized, medium-grained granodiorite with intense Bt-Ser-Chl alteration associated with Py-Cpy mineralization and  $V_{2b}$  vein.

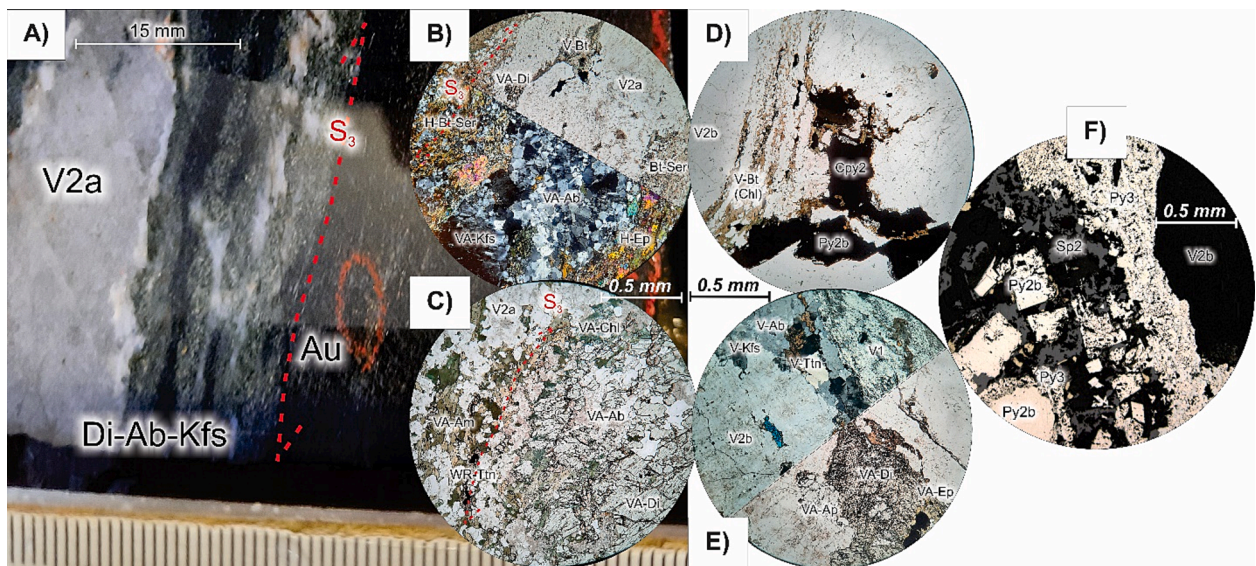


**Fig. 7.** (A)  $V_{2a}$  Di-Ab-Qz vein cutting sheared Chl-Hbl-Bt schist (21DBS-09) concordant to foliation with minor foliation-parallel, disseminated, fine-grained Py and trace gold mineralization. (B)  $V_{2a}$  Kfs-Ab-Qz vein concordantly cutting Bt-dominated shear band within a Chl-Hbl-Bt schist (20DBF-8B). (C) Ab-Qz-Di  $V_{2a}$  vein cutting Chl-Bt-Hbl schist with vein-adjacent Chl, Am, and Di alteration. (D).  $V_{2b}$  vein within a Bt-schist (20DBF-7B) with V-Bt and V-Chl forming around  $Py_{2b}$  and  $Cpy_2$  mineralization. (E) Contact between deformed  $V_1$  and recrystallized  $V_{2b}$  hosting VA-Ap, VA-Di, VA-Ep, and V-Ttn within a Chl-Hbl-Bt schist (20DBF-14). (F)  $Py_{2b}$ - $Py_3$ - $Sp_2$ - $Cpy_2$  and minor Gn mineralization hosted within a  $V_{2b}$  vein that cuts a sheared tonalite (21DBS-04).

property and Santoy Mine Complex. The gradational nature between the distal halo and proximal assemblages and semi-concordant orientation with quartz veins and  $S_3$  foliation defined by shearing suggest coeval development during *syn*-late- $D_3$  deformation. The relative timing of these alteration assemblage agrees with the synonymous distal and proximal alteration assemblages present within Assemblage A rocks, suggesting formation under similar and semi-coeval conditions.

The characteristics of the vein-adjacent alteration assemblage in intrusive rocks are similar between the Fisher property and Santoy Mine Complex. The alteration assemblage yields a semi-concordant relationship with quartz veins and  $S_3$  foliation, implying generation during continuous *syn*-late- $D_3$  deformation, slightly subsequent to the distal halo and proximal alteration assemblages and under semi-coeval conditions to the vein-adjacent assemblage in Assemblage A rocks. In

contrast to Santoy samples, Fisher samples show a considerably more intense grain size reduction between alteration assemblages, and is likely the result of more intense shearing within the tighter portion of the shear corridor.

#### 4.3. Vein classification

The veins that cut both the sheared Assemblage A and intrusive units are variable, both in composition and in relative timing (Fig. 7A–E). The earliest veins ( $V_1$ ; Fig. 7E) are present as cm- to m-scale extensively deformed quartz mylonite, semi-concordant to foliation, and comprising quartz (85–90 %), rotated pyrite and pyrrhotite (<5–5 %), biotite-chlorite stringers (5–10 %), and feldspar augens (<5%). Locally, these veins are crosscut by subsequent vein generations. Based on the extensive deformation, rotated clasts, and feldspar augens present in  $V_1$  veins, coupled with the crosscutting nature of subsequent vein generations and moderately foliation-concordant occurrence this vein set is interpreted to have developed primarily early-to syn- $D_3$ .

The most prevalent veins present at the Fisher property and Santoy Mine Complex are thin (0.12 mm–3 cm) quartz-albite  $\pm$  diopside-sulfide-K-feldspar-carbonate veins ( $V_{2a}$ ; Fig. 7A–C) and large (m-scale) recrystallized quartz  $\pm$  sulfide veins ( $V_{2b}$ ; Fig. 7D–F).  $V_{2a}$  veins are typically weakly to moderately deformed, semi-concordant to foliation, and occasionally boudinaged and weakly crenulated. These veins typically comprise mosaic-textured quartz (60–95 %), albite (10–25 %), and variable amounts of K-feldspar (<5–10 %), diopside (<5–10 %), pyrite (<5–15 %), chalcopyrite (<5–5 %), magnetite (<5%), sphalerite (<5%), and pyrrhotite (<5–10 %). Additionally, within these veins there are thin biotite-chlorite stringers, acicular actinolite, minor interstitial calcite, coarse-grained diopside and apatite, and euhedral titanite, where biotite and chlorite typically form along the edges of sulfide minerals (Fig. 7B).  $V_{2b}$  veins are larger, semi-concordant to foliation, and dominantly comprised of mosaic-textured quartz. Within these veins there is a variable amount of chloritized and diopside-actinolite-altered wall rock fragments, biotite-chlorite stringers, coarse titanite and apatite, and sulfide mineralization (Fig. 7D–F). Similarly, biotite-chlorite-actinolite alteration is present on the edges of sulfide minerals (Fig. 7D). Mineralization in these veins generally comprise pyrite (5–15 %), pyrrhotite (5–15 %), chalcopyrite (<5–5 %), and magnetite (<5–5 %), where sphalerite, galena, and chalcopyrite content increase in  $V_{2b}$  veins that cut intrusive rocks (Fig. 7F), suggesting that metal remobilization within intrusive sample was present.

The similarities between the characteristics of alteration, and proximity between  $V_{2a}$  and  $V_{2b}$  quartz veins as well as association with the calc-silicate alteration assemblage, suggest that these veins are roughly coeval and interpreted to have developed during syn- to late- $D_3$  deformation.  $V_{2a}$  veins, which frequently develop proximal to  $V_{2b}$  veins, are interpreted to have manifested in thin fluid pathways adjacent to  $V_{2b}$  veins, as opposed to being a distinct generation. Contrastingly,  $V_1$  veins that lack rotated clasts and feldspar augens could potentially be representative of non-recrystallized  $V_{2b}$  veins. As such, these vein generations likely represent main-stage gold mineralization spanning from syn- to late- $D_3$  deformation and are likely synonymous across all lithologies.

A late set of veins ( $V_3$ ) is evident across the Seabee Gold Operation, manifesting as thin (~0.5 cm) quartz or carbonate-quartz veins. These veins dominantly comprise quartz or pink-stained carbonate with minor quartz, both of which are associated with adjacent K-feldspar alteration and hematization. These veins crosscut the altered wall rock, as well as  $S_3$  foliation and previous vein generations at a 30–60° angle and are present at the surface with roughly an east–west trend. Although rare, these veins are also observed with minor chalcopyrite-pyrite mineralization. This vein set, which crosscuts foliation, previous vein generations, and fill brittle fractures are interpreted to have developed under brittle conditions during  $D_4$  deformation.

#### 4.4. Alteration mineral phases and associated chemistry

A paragenetic sequence (Fig. 8) was constructed to summarize the above observations and facilitate the characterization of elemental variations associated with hydrothermal alteration and sulfide-gold mineralization. As such, the results of electron microprobe analyses on these mineral phases are described below.

##### 4.4.1. Feldspar

The occurrences of K-feldspar and plagioclase are intimately associated with one another and similar between the Fisher and Santoy properties. These phases were identified as (i) WR-, hosted within the distal halo assemblage either within the groundmass in meta-basalt and schists (Fig. 5A, E) or as medium-grained phenocrysts in intrusive rocks (Fig. 6C, E), both occurring amongst foliated biotite-chlorite-amphibole; (ii) H-, occurring as fine-grained alteration as thin ~0.12–1.25 mm bands within the distal halo and proximal assemblages in schists and intrusive rocks (Fig. 5F); and (iii) VA- coarse-grained, anhedral alteration within the vein-adjacent calc-silicate alteration of schists (Figs. 5D and 7E).

Chemical compositions of plagioclase and K-feldspar are present in Appendix B. In terms of K-feldspar, minimal chemical variation is present between WR- and VA- phases, where unaltered compositions record  $An_{0.0}-Ab_{0.07-0.06}-Or_{0.93-0.92}$ . Although H- phases of K-feldspar in mafic volcanic rocks show limited variability versus their altered equivalent ( $An_{0.0}-Ab_{0.08}-0.06-Or_{0.94-0.92}$ ), H- phases in granodiorite exhibit minor element variability, including more Na-rich compositions ( $An_{0.0}-Ab_{0.06-0.01}-Or_{0.99-0.94}$ ) in altered granodiorite (Agrd). VA- phases, associated with quartz veins, calc-silicate alteration, and potential sulfide-gold mineralization, comprises variable compositions ( $An_{0.0}-Ab_{0.11-0.06}-Or_{0.94-0.89}$ ), however, minor element variability, including more Na-rich compositions is weakly evident throughout the entirety of the samples (Fig. 9A). In WR- phases, notable impurities comprise FeO (0.16–0.17 wt %) and BaO (0.74–2.58 wt%), whereas in VA- phases, BaO is the only main impurity (0.65–1.19 wt%).

In contrast, there is a weak trend from labradorite-andesine plagioclase varieties in unaltered rocks to albite plagioclase in altered rocks (Fig. 9A). In mafic volcanic samples, WR-plagioclase compositions record andesine chemistry ( $An_{0.41-0.33}-Ab_{0.66-0.58}-Or_{<0.01}$ ), and a previously analyzed high-chromium unaltered basalt from the Fisher property yields a labradorite chemical composition ( $An_{0.58}-Ab_{0.41}-Or_{<0.01}$ ) (Onstad, 2021). VA- phases, associated with calc-silicate alteration and sulfide-gold mineralization typically yield albite mineral chemistry ( $An_{0.14-0.07}-Ab_{0.99-0.85}-Or_{<0.01}$ ), with intermediary H-phases plotted within the andesine-oligoclase field. Notable impurities include FeO (0.07–0.16 wt%) and SrO (0.05–0.15 wt%) in WR- and FeO (0.03–0.39 wt%) in VA-plagioclase phases, respectively. The chemical transition from labradorite-andesine to albite plagioclase compositions associated with alteration is weakly uniform among the Fisher and Santoy samples, and has been recognized in other orogenic gold systems (Goldfarb et al., 2005).

##### 4.4.2. Amphibole

The Fisher and Santoy properties yield variable occurrences of analyzed amphibole phases (Appendix B). These phases were identified in meta-basalts and schists as (i) WR-, strongly foliated, subhedral, fine- to medium-grained porphyroblasts within the unaltered assemblage (Fig. 5A, E); (ii) H-, foliated, medium-grained, subhedral rhombic crystals that are weakly chloritized and occur within the distal halo assemblage (Fig. 5F); (iii) VA-, adjacent to calc-silicate alteration, quartz veins, and sulfide mineralization, as medium-grained, euhedral bladed to acicular crystals with green-light green pleochroism within the proximal to vein-adjacent assemblage (Figs. 5G and 7C); and (iv) V-, chloritized, medium-grained, euhedral acicular crystals, locally forming fibrous aggregates hosted within  $V_{2a}$  and  $V_{2b}$  veins (Fig. 5H). These identified amphibole phases include both coexisting calcic and Ca-Mg-

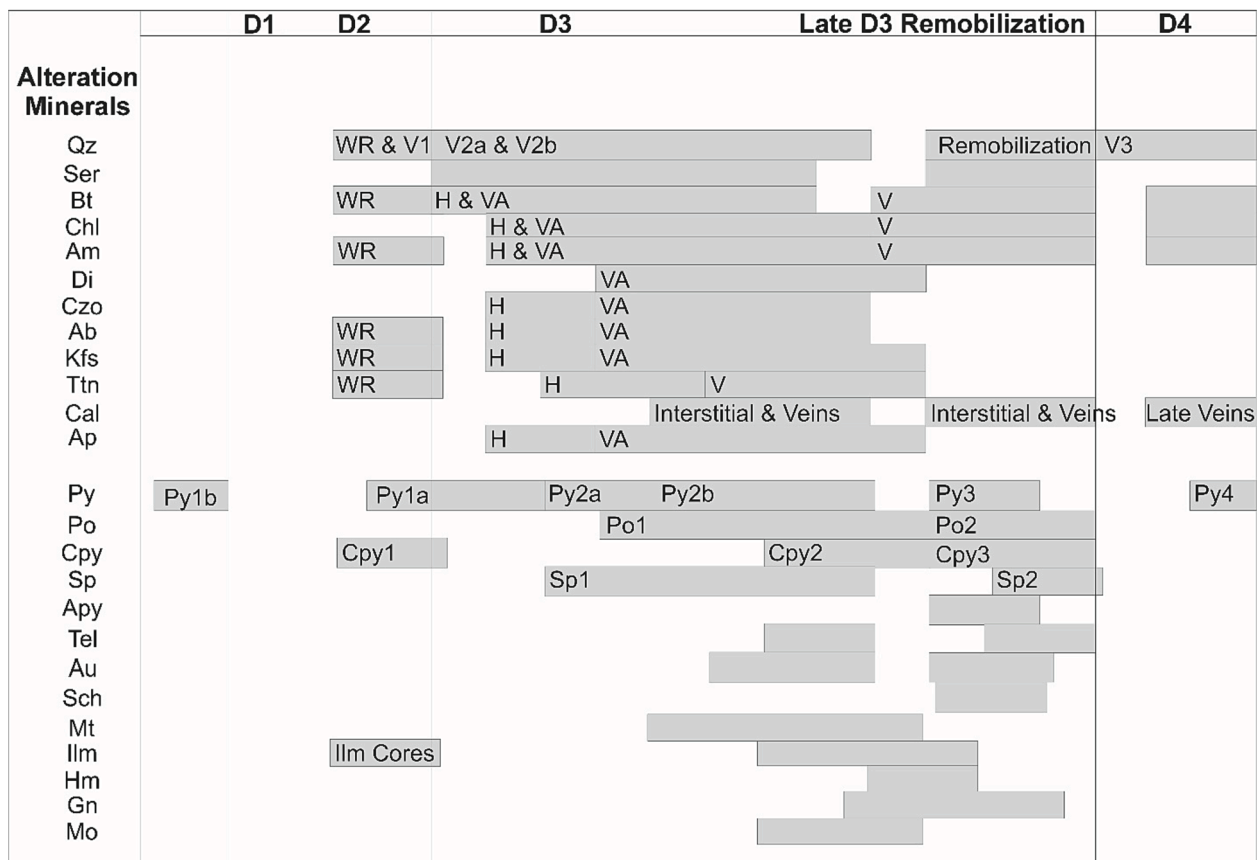


**Fig. 8.** Paragenetic sequence developed for the Fisher and Santoy samples, comprising sulfide minerals, metals, silicates, and alteration minerals. Prefixes denote mineral phases as WR- wall rock, in altered and representative wall rock; H- halo, associated with halo alteration and shearing within the distal halo assemblage; VA- vein-adjacent, directly adjacent to V<sub>2a</sub> and V<sub>2b</sub> veins within the proximal and vein-adjacent calc-silicate assemblage; V- vein, hosted within V<sub>2a</sub> and V<sub>2b</sub> veins or within the vein-adjacent assemblage.

Fe-Mn-Li groups that occur amongst each other and are subsets of the calcic amphibole supergroup. It is important to note that although calcic amphiboles share similar WR- to VA- occurrences to the Ca-Mg-Fe amphiboles, the former occur in higher grade host rocks in closer spatial proximity to a higher density of quartz-sulfide-gold veins (m-scale). These parameters for the classification of amphibole subgroups are as follows:  $Ca^B \geq 1.50$ ,  $(Na + K)^A \geq 0.50$ , and  $Ti < 0.50$  for calcic, and  $Ca^B \geq 1.50$ ,  $(Na + K)^A < 0.50$ ,  $Ca^A < 0.50$  for Ca-Mg-Fe amphiboles (Leake et al., 1997).

In terms of both the Ca-Mg-Fe and calcic amphibole groups, chemical compositions vary between WR- and V- phases associated with increased intensity of alteration and mineralization. For Mg-Fe amphiboles, WR-amphibole phases primarily occur within the Mg-hornblende field (Table 2). The H- and VA- phases yield a wide distribution, weakly trending from Mg-hornblende to Actinolite, however V-phases dominate the latter (Table 2). In general, the trend from Mg-hornblende to actinolite is weakly related to increasing alteration and proximity to veins and sulfide mineralization in primarily Fisher amphiboles and some Santoy samples (Fig. 9B), associated with a slight increase in Mg and decrease in K, Na, Fe, and Al.

For calcic amphiboles, mineral chemistry ranges from edenite to ferro-pargasite compositions, with single occurrences of pargasite and ferro-edenite. The unaltered WR- phases primarily consist of edenite mineral chemistry (Table 2). Although there is no occurrence of calcic V-phases, amphibole compositions weakly shift to ferro-paragastie, defined primarily by VA- phases (Table 2, Fig. 9C). In contrast to Ca-Mg-Fe amphiboles, the calcic amphibole chemistry shows an increase in Ca, Fe, and Al and a decrease in Mg associated with alteration. These elemental variations, which are opposite to those defined by Ca-Fe-Mg

amphiboles, potentially suggests the presence of continuous hydrothermal processes during the same relative hydrothermal event. As the trend in calcic amphiboles related to alteration is defined more by Santoy amphiboles, these continuous hydrothermal processes would have been more prevalent at the Santoy Mine Complex.

#### 4.4.3. Chlorite

The Fisher and Santoy samples yield similar chlorite compositions (Appendix B) and show weak chemical trends associated with alteration and sulfide-gold mineralization. Chlorite phases were identified as (i) H-, within the distal halo alteration assemblage and shear bands, occurring as fine- to medium-grained, foliated, subhedral crystals, or as chloritization at the edge of Bt-shear bands within schists (Fig. 4A–C, E); (ii) VA-, adjacent to sulfide mineralization, V<sub>2a</sub> and V<sub>2b</sub> veins, or within the calc-silicate alteration assemblage as fine- to medium-grained an-subhedral crystals in the proximal to vein-adjacent assemblages in schists and intrusive rocks (Figs. 5C, D and 6D); and (iii) V-, within V<sub>2a</sub> and V<sub>2b</sub>, or fracture-filling, as fine- to medium-grained, an-subhedral crystals or chloritization of wall rock fragments within schists (Fig. 5B).

There are weakly similar chemical trends between the Fisher and Santoy samples, where less altered intermediate-clinoclchlore compositions shift toward the Fe-rich chamosite endmember (Fig. 9D), all of which are type I ( $Mg + Fe > Al + Q$ ), with increasing alteration. For H-phases, compositions comprise intermediate-clinoclchlore mineral compositions (Table 2). The VA- phases exhibit a transitional distribution to V- phases, which are indicative of chamosite compositions (Table 2). Notable impurities include Na and Ca, which reach up to 0.12 wt% and 0.11 wt% in H-phases, respectively, as well as Cl which increases slightly in V- phases (up to 0.04 wt%). As such, these mineralogical changes in

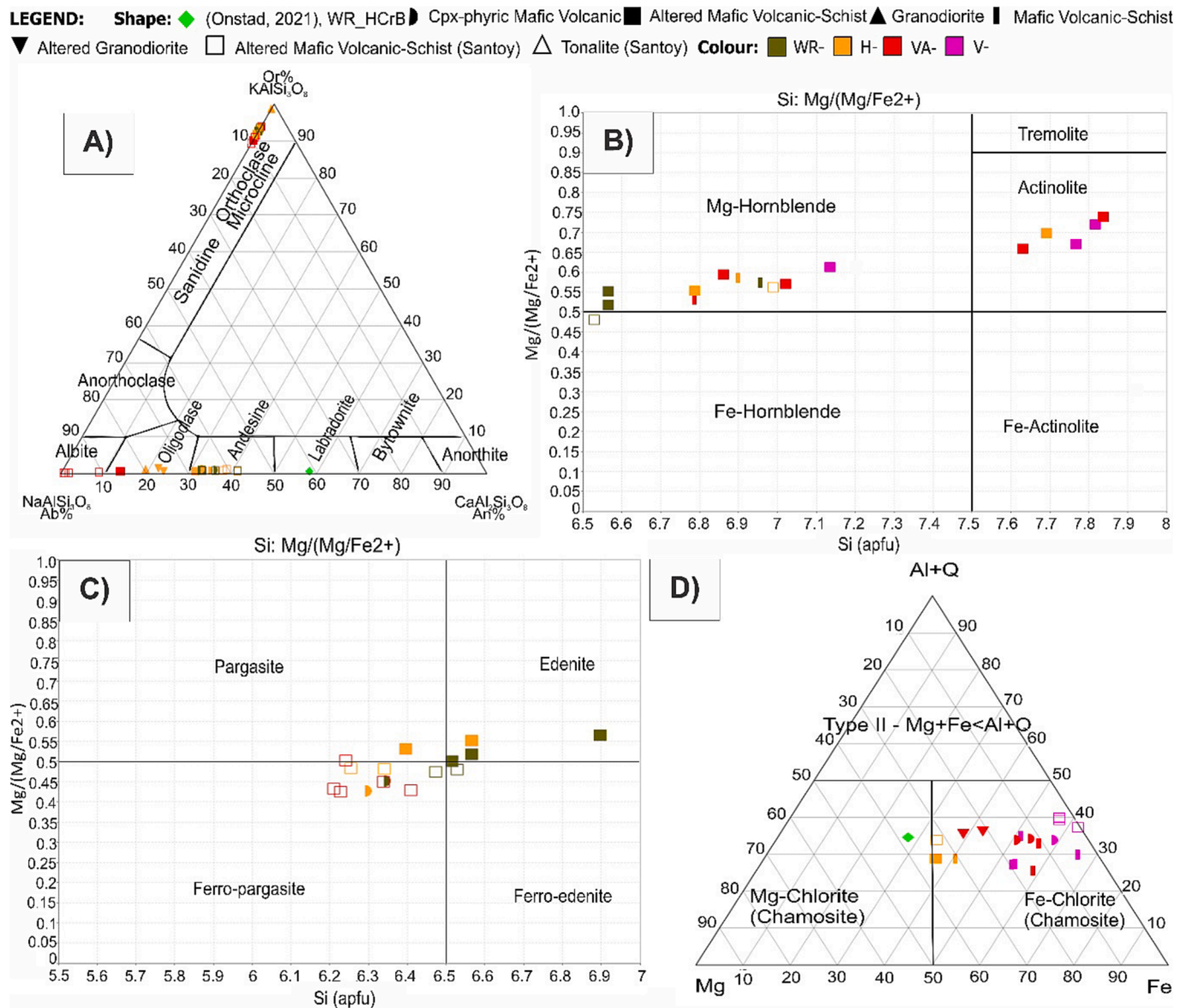


**Fig. 9.** Mineral chemistry diagrams using atoms per formula unit (apfu) of respective mineral phases from meta-basalts, schists, and intrusive units. (A) ternary classification diagram for feldspars (Deer et al., 1998). (B) Ca-Mg-Fe-Mn-Li amphibole classification diagram (Leake et al., 1997). (C) Calcic amphibole classification diagram (Leake et al., 1997). (D) Ternary (Al + Q)-Mg-Fe classification diagram for chlorite (Zane and Weiss, 1998).

Fisher and Santoy chlorites correspond to an increase in Fe and  $Al^{IV}$ , decrease in Mg, Mn, and variable  $Al^{TOT}$  and Q associated with increased alteration and mineralization.

#### 4.4.4. Biotite

Similar phases and corresponding elemental variations were identified between Fisher and Santoy biotite phases. These phases include (i) WR-, foliated and crenulated, brown, subhedral, fine- to medium-grained crystals within unaltered sections of meta-basalt groundmass (Fig. 5A, E); (ii) H-, strongly foliated and crenulated, sub-euhedral, medium-grained crystals with brown-slightly red pleochroism within this distal halo assemblage and shear bands of schists (Figs. 4E, 5B, and 7B); (iii) VA-, juxtaposed against the calc-silicate assemblage, sulfide mineralization, and quartz veins, occurring as medium-grained, an-subhedral crystals with deep brown-red pleochroism and more random orientations within the proximal and vein-adjacent assemblages of schists and intrusive rocks (Fig. 5G and 6F); and (iv) V-, medium- to coarse-grained, sub-euhedral crystals within fractures, the calc-silicate alteration assemblage,  $V_{2a}$  and  $V_{2b}$  veins, or adjacent to

mineralization, with light brown-red pleochroism and crosscutting orientations within schists (Fig. 7D).

The process developed by Li et al. (2020) was used for calculations (Appendix B), and a weakly similar trend from Fe-biotite to Mg-biotite, towards phlogopite, was identified in Fisher and Santoy samples (Fig. 10A). Less altered WR- phases typically comprise Fe-biotite that approaches the siderophyllite field, however, a WR- phase from Santoy yields Fe-Mg-biotite (Table 2). H- and VA- phases share similar compositions, however a slight trend toward Mg-biotite compositions is present. V- phases, associated with  $V_{2a}$  and  $V_{2b}$  veins, calc-silicate alteration, and specifically form around the edges of vein-hosted sulfide minerals comprises Mg-biotite mineral chemistry (Table 2). In summary, biotite associated with alteration and mineralization exhibit a minor increase in Mg, Al and Ti and a decrease in Fe.

#### 4.4.5. Other mineral chemistry analyses

Other elemental variations (Fig. 10B–D) were identified in alteration minerals at Fisher and Santoy, the analyses of which are made available in Appendix B. Similar phases of titanite were recognized for Fisher and

**Table 2**  
Chemical composition (apfu) ranges of Fisher and Santoy amphibole, chlorite, and biotite mineral phases. <sup>F</sup> Fisher sample; <sup>S</sup> Santoy sample.

Mineral Phase	Chemical Composition												
	[K <sup>A</sup> ]	Na <sup>A</sup>	[Ca <sup>B</sup> ]	Mn	[Mg]	Fe <sup>3+</sup>	Fe <sup>2+</sup>	Al <sup>VI</sup>	Ti	Cr	[Si]	Al <sup>IV</sup>	
Mg-Fe Am	WR	0.22-0.14	0.37-0.26	1.95-1.89	0.07-0.06	2.60-2.31	0.42-0.22	1.93-1.88	0.32-0.23	0.07-0.03	0.02-0	6.99-6.57	1.44-1.01
	V	0.02-0.01	0.06	1.95-1.93	0.08-0.05	3.51-3.25	0.09-0.06	1.59-1.37	0.06-0.04	0.01	0	7.82-7.77	0.23-0.18
	VA	0.35-0.28	0.43-0.36	1.93-1.89	0.08-0.07	2.91-2.13	0.39-0.34	2.12-2.04	0.34-0.32	0.09-0.07	0	0	1.49-1.43
Calcic Am	WR	0.35-0.28	0.43-0.36	1.97-1.92	0.06-0.05	1.83-1.74	0.29-1.18	2.44-2.29	0.54-0.44	0.12	0	0	1.79-1.60
	H	2.42-1.99	5.49-4.84	5.41-4.16	0.07-0.06	2.30-1.61	6.39-5.70	0.30-0.11					
	V	2.05-1.90	8.93-7.07	2.60-0.57	0.05-0.04	2.61-1.32	6.69-6.38	0.40-0.20					
Bt	WR <sup>F</sup>	0.93-0.88	0.01	0.45-0.44	0.96-0.86	1.37-1.32	0.55-0.43	0.07	0.02	2.75-2.74	0.92-0.89		
	WR <sup>S</sup>	0.94	0.02	0.42	1.23	1.02	0.30	0.13	0.02	2.78	1.01		
	V	0.96-0.94	0.02-0.01	0.39-0.35	1.57-1.43	0.89-0.74	0.24-0.19	0.13-0.12	0.02	2.80-2.77	1.09-1.06		
	[K]	Na	[Al <sup>VI</sup> ]	Mg	Fe <sup>2+</sup>	Fe <sup>3+(MTD)</sup>	Ti	[Si]	Mn	Al <sup>IV</sup>			

Santoy samples, which show distinct morphologies between phases, but minimal chemical variation (Figs. 5A, F, H, and 7E), where Ti, Al, Fe, and Ca vary only by a few wt% between WR- and V- phases (Fig. 10C). Although clinopyroxene in samples was determined to be dominantly diopside (Fig. 10B), which occurs in the vein-adjacent assemblage associated with mineralization (Fig. 5H). In terms of apatite, WR- to VA phase compositions occupy the fluorapatite field and yield variations that shift to F-rich compositions (from 0.72 to 0.99 apfu). Additionally, BiTe mineral phases were identified to comprise tetradyrite (Bi<sub>2</sub>Te<sub>2</sub>S) which typically forms around a tellurobismuthite (Bi<sub>2</sub>Te<sub>3</sub>) or gold core (Fig. 10D).

#### 4.5. Mineralization and sulfide mineral phases

The sulfide minerals and their paragenetic relationship with other alteration minerals (Fig. 11A-F) are similar between the Fisher and Santoy properties (Fig. 8; Appendix A). Their textural relationships and chemistry are described in detail in Beaudin et al. (in review) but are summarized here. In schists and intrusive lithologies, sulfide minerals are dominated by subhedral, pitted, replacement-style Py<sub>2a</sub> mineralization with Cpy<sub>1</sub>-Bt < Pl < Sp<sub>1</sub>-Mt-Po<sub>0</sub>-Ilm inclusions, occurring concordant to S<sub>3</sub> foliation within the alteration assemblages and quartz veins (Fig. 11A, C, F). Py<sub>2b</sub> and associated phases are observed cross-cutting and forming around Py<sub>2a</sub> and earlier phases (Fig. 11A, F), however, an-subhedral Po<sub>1</sub> and Cpy<sub>2</sub> are observed overprinting the former (Fig. 11A, F). The occurrence of these phases within the distal halo, proximal, and locally vein-adjacent alteration assemblages, concordance to S<sub>3</sub> foliation, and association with free, fine-grained, disseminated gold-telluride minerals suggests a *syn*-late-D<sub>3</sub> timing for mineralization (Fig. 8). As such, these sulfide phases and associated gold mineralization define the onset of main-stage orogenic-style gold mineralization during *syn*-late-D<sub>3</sub> deformation. Additionally, anhedral (locally euhedral), inclusion-rich, sieve-textured, pitted, fine-grained Py<sub>3</sub> overprints earlier sulfide phases in schists and intrusive rocks. This phase is associated with Po<sub>2</sub> and Cpy<sub>3</sub> that have similar textures and primarily (i) fills foliation-parallel fractures or is concentrated within fractured competent grains, such as diopside, within the calc-silicate alteration assemblage (Fig. 5H); and (ii) is associated with free gold-telluride mineralization. Py<sub>3</sub>-Po<sub>2</sub>-Cpy<sub>3</sub> and associated gold mineralization thus portray characteristics of remobilization, and precipitated within vein-adjacent calc-silicate alteration assemblage during fracturing from continuous late-D<sub>3</sub> deformation. Consequently, these sulfide phases and associated gold mineralization represent the cyclical nature of gold deposition related to multiple fluid events during D<sub>3</sub> deformation (Fig. 8).

In terms of earlier pyrite generations, similar mineralization characteristics are observed, in intrusive rocks, however, the mentioned phases occur primarily adjacent to or within V<sub>2a</sub> and V<sub>2b</sub> veins (Fig. 11F), suggesting formation akin to those present within Assemblage A rocks. Sulfide minerals in Assemblage A and intrusive rocks are typically similar. However, a deformed, inclusion-rich (Qz-Pl-Ilm-Cpy-Mt), sub-euhedral, replacement-style, pitted, fractured, fine- to medium-grained Py<sub>1b</sub> phase (Fig. 11B, E) is observed disseminated throughout the alteration assemblages of intrusive samples. The isolated occurrence within intrusive samples and early paragenetic relationship with other phases suggests the crystallization of this phase preceded D<sub>3</sub> deformation (Fig. 8). Additionally, relict, grainy subhedral-cubic or euhedral-colloform Py<sub>1a</sub> (Fig. 11C) is locally observed and overprinted by Py<sub>2</sub> and subsequent phases within schists. The colloform nature of this phase implies crystallization from likely supersaturated fluids (Barrie et al., 2009, Atanassova, 2010, Shang et al., 2016). The textures and timing of Py<sub>1a</sub> and Py<sub>1b</sub> suggests the potential for introduction of gold-bearing fluids into the system prior to or during early-D<sub>3</sub> deformation.

**LEGEND:** Shape: ◆ (Onstad, 2021), WR\_HCrB ▾ Cpx-phyrlic Mafic Volcanic ■ Altered Mafic Volcanic-Schist ▲ Granodiorite ▮ Mafic Volcanic-Schist  
▼ Altered Granodiorite □ Altered Mafic Volcanic-Schist (Santoy) △ Tonalite (Santoy) Colour: ■ WR- ■ H- ■ VA- ■ V-

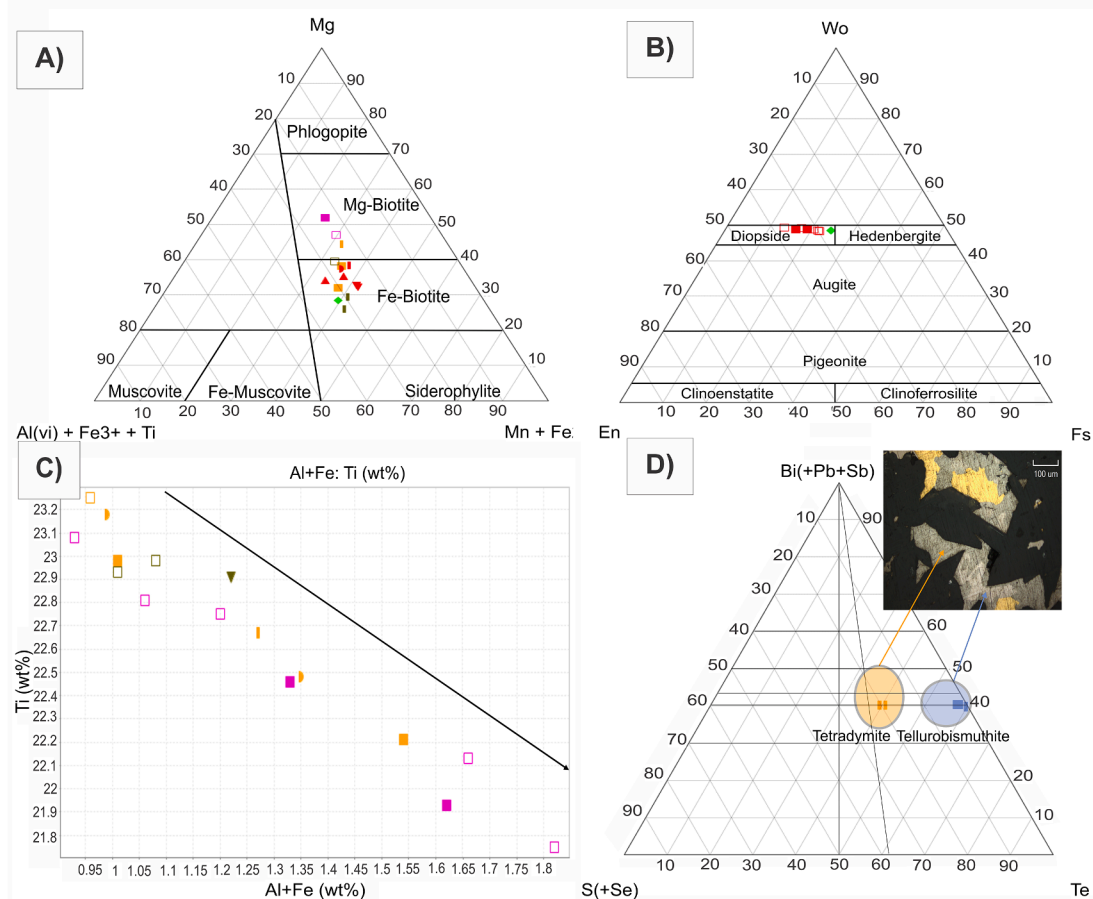


**Fig. 10.** Mineral chemistry diagrams using atoms per formula unit (apfu) of mineral phases from meta-basalts, schists, and intrusive lithofacies. (A) Ternary classification of biotite from Foster (1960). (B) Clinopyroxene ternary classification diagram (Morimoto, 1988). (C) Al + Fe:Ti biplot for titanite. (D) Telluride-group mineral discrimination diagram (Cook and Ciobanu, 2004) and associated representative photomicrograph.

## 5. Discussion

### 5.1. Composition of alteration minerals and constraints on formation conditions

Similar mineralogy and changes in mineral chemistry are observed between the Fisher property and Santoy Mine Complex associated with progressive alteration and associated sulfide-gold mineralization. Fisher and Santoy plagioclase show a trend in composition related to alteration from andesine-labradorite WR-phases to albite VA-phases. This increase in Na-compositions and occurrence of albite associated with alteration has been identified in numerous orogenic gold systems (e.g., Groves et al., 2020). Amphiboles in both Fisher and Santoy samples yield compositional trends from Mg-Hbl to Act, with a weak trend from edenite to ferropargasite and stronger trend from ferroedenite to ferropargasite at Fisher and Santoy, respectively. This mineralogical variation is likely explained by concurrent fluid events, generating a compositional shift from Mg-Hbl to Act at both Fisher and Santoy during early alteration, followed by a later fluid flux from which ferropargasite in Fisher and, to a greater degree, in Santoy samples precipitated. This evidence for an increased exposure to cyclical fluid fluxes (Sibson et al., 1988) at Santoy during D<sub>3</sub> deformation and main-stage gold-mineralizing event, could provide justification for the higher grade of mineralization observed at that location, which would also have been remobilized and locally concentrated during late D<sub>3</sub> (McCuaig and Kerrich, 1998). Furthermore, this shift from hornblende to actinolite

compositions associated with alteration has been observed in numerous orogenic gold systems (e.g., Mueller, 1992, Samson et al., 1999, Zhao et al., 2019, de Souza et al., 2021), and actinolite has been observed in numerous alteration assemblages in the La Ronge domain (Komis: Asbury, 1986, Lafrance, 2000; Jolu: Thomas and Heaman, 1994; Tower East: Simpson, 2006). The compositional trend from Fe- to Mg-Bt coupled with a shift in composition from Mg- to Fe-Chl has also been recognized in multiple orogenic gold systems (e.g., Mueller, 1992, Samson et al., 1999, Gaillard et al., 2018, De Souza et al., 2019, Groves et al., 2020, de Souza et al., 2021).

To provide temperature constraints on the conditions of alteration, calculations using chlorite geothermometers were made using phases from the distal halo and vein-adjacent assemblages at the Fisher and Santoy properties. Since Fe/(Fe + Mg) values presented by (K) Kranidiotis and MacLean (1987) are compatible with some of the Fisher and Santoy chlorites and used in other studies on orogenic gold systems (e.g., de Souza et al., 2021), this geothermometer was chosen, although the V-Chl phases reach the upper limit of the mentioned ratio. As such, the geothermometers of (C) Cathelineau (1988) and (Z) Zang and Fyfe (1995) were also tested and discussed below. Generally, the geothermometers presented by (K) and (C) agree across all phases (standard deviation of ~48 and 44 °C for H and VA-V, respectively), and represent the maximum and minimum of the presented temperatures ranges, respectively. The calculated temperature of formation for H-Chl was determined to be 260–270 °C within the distal halo alteration assemblage and 320–330 °C for VA- and V-Chl within the proximal to vein-

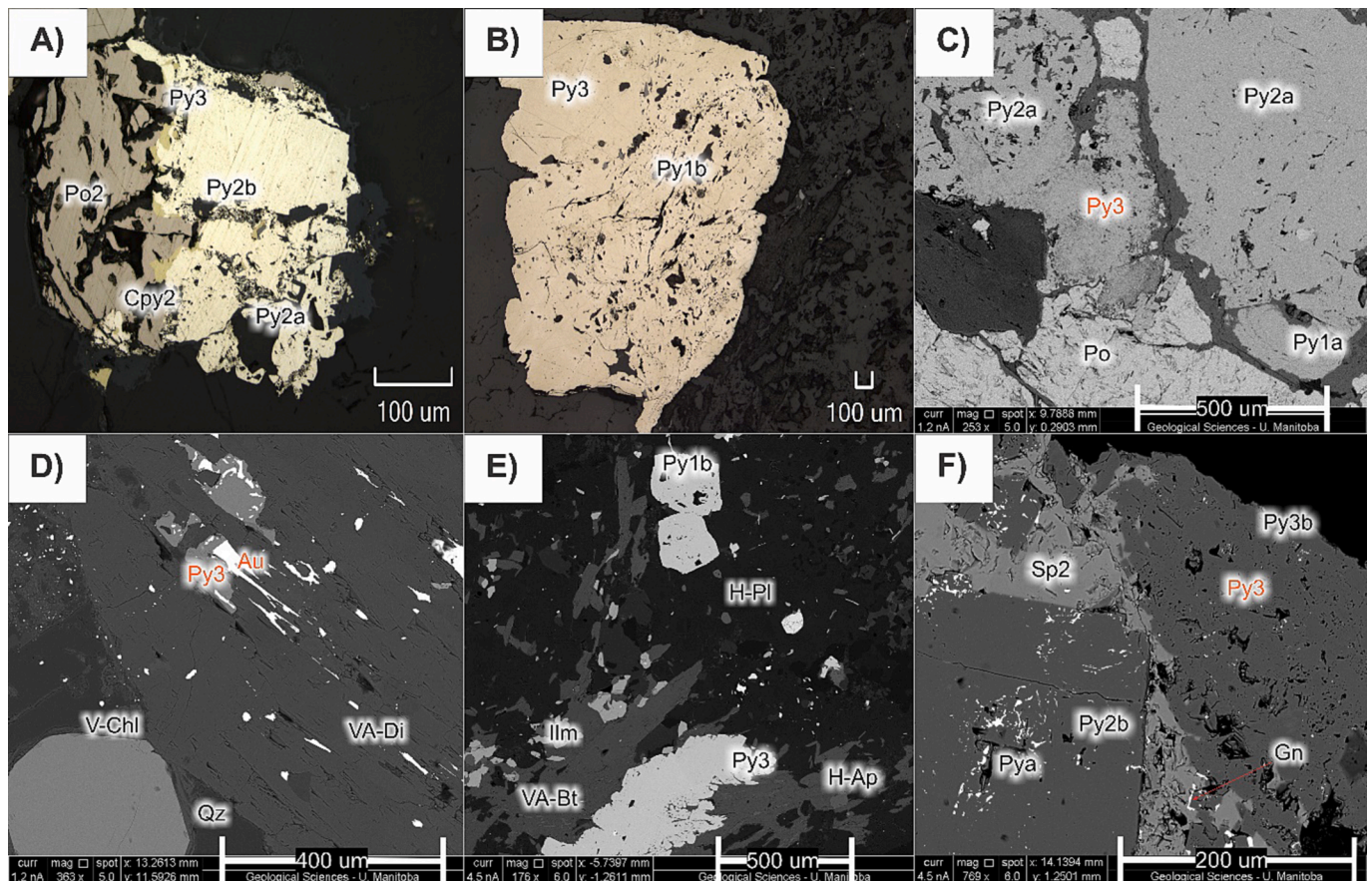


**Fig. 11.** Photomicrographs and back-scattered electron images showing multiple stages of sulfide mineralization in mafic volcanic and intrusive samples. (A) Py<sub>2a</sub> overprinted by Py<sub>2b</sub> and Py<sub>3</sub> forming around the edges of earlier phases (Po<sub>2</sub> and Cpy<sub>2</sub> which form around Py<sub>2</sub>) (20DBF-13B). (B) Porous, inclusion-rich Py<sub>1b</sub> with Py<sub>3</sub> forming along the edges (20DBF-10A). (C) Porous Py<sub>2a</sub> overprinting colloform Py<sub>1a</sub> with Py<sub>3</sub> forming along the grain boundaries and overprinting Po within a sulfide lens (20DBF-24). (D) fracture-filling Py<sub>3</sub> associated with gold mineralization adjacent to V<sub>2b</sub> vein (20DBF-1A). (E) Inclusion-rich Py<sub>1b</sub> core with Py<sub>2b</sub> forming along the outside adjacent to a V<sub>2b</sub> vein (20DBF-10A). (F) V<sub>2b</sub> vein hosting Py<sub>2b</sub> with Py<sub>2a</sub> cores with Py<sub>3/3b</sub> forming along the edge associated with Sp<sub>2</sub> and Gn (21DBS-04).

adjacent assemblages, associated with sulfide-gold mineralization (Appendix B). These values are ~30–100 °C hotter than those calculated using the formula outlined by (Z). This under-estimation of temperature likely stems from the calibration and resulting correction (Z) applied to Chl with high XFe values (0.78–0.81), of which occupies a small range of values present in Fisher and Santoy chlorite. These proposed crystallization temperatures for gold-associated VA- and V-Chl agree with the 300 ± 50 °C formation conditions expected for orogenic gold deposits (Goldfarb and Groves, 2015).

Similarly, empirical calculations were completed to ascertain pressure conditions of alteration and associated sulfide-gold mineralization. Uchida et al. (2007) determined a positive correlation between Al<sub>tot</sub> and the estimated pressure conditions during the formation of biotite in hydrothermal processes. H-Bt within the distal halo alteration assemblage yields a value of about 2 kbar, corresponding to a depth of about 7 km according to Willson (2010). Additionally, the pressure estimates for VA- and V-Bt within the proximal to vein-adjacent assemblage and associated with calc-silicate alteration and sulfide-gold mineralization is around 3 kbar with an equivalent depth of 9 km (Willson, 2010; Appendix B). These pressure conditions and associated depths during the crystallization of gold-associated VA- and V-Bt from hydrothermal fluids corresponds to the proposed range of pressures and depths for orogenic gold deposit formation of 1.5 ± 0.5 kbar and 4–15 km depth at the transitional ductile–brittle boundary (Goldfarb and Groves, 2015, Groves et al., 2020).

The temperature and pressure ranges of Fisher and Santoy generally agree (Fisher: ~310–320 °C, 3 kbar; Santoy: ~360 °C, 2–3 kbar).

Furthermore, these determined hydrothermal conditions are comparable to the results of fluid inclusion studies of quartz at the Seabee deposit by Tourigny et al. (2004), which identified homogenization temperatures and pressures of about 370 °C and 1.1–2.5 kbar from paired liquid-rich and vapour rich aqueous-carbonic fluid inclusions. In contrast, the vein-adjacent calc-silicate alteration assemblage, specifically diopside, and K-feldspar, suggests the involvement of higher temperature hydrothermal fluids (~525 °C; McCuaig and Kerrich, 1998). Although this high temperature calc-silicate alteration assemblage is atypical of orogenic gold systems, the Chalice deposit in the Yilgarn craton (Bucci et al., 2004) provides an example of such an occurrence.

In summary, the similar mineralogical variations and trends associated with progressive alteration and mineralization in Fisher and Santoy host rocks suggests a closely related hydrothermal system. These elemental variations and trends are similar to those present in other orogenic gold systems, and as such, provide support for orogenic-style mineralization. Furthermore, the thermal conditions (~320–330 °C) determined for the formation of VA- and V-Chl, as well as the pressure conditions and determined depth during the crystallization VA- and V-Bt (~3 kbar and ~9 km depth) are also consistent with fluid conditions proposed for orogenic gold systems (300 ± 50 °C; 1.5 ± 0.5 kbar, 4–15 km depth; (Goldfarb and Groves, 2015, Ridley and Diamond, 2020). Consequently, both the Fisher property and Santoy Mine Complex likely have undergone analogous hydrothermal events attributed to a regional-scale orogenic gold-mineralizing system in which metamorphic devolatilization reactions at the greenschist-amphibolite grade transition (Goldfarb and Groves, 2015) generated fluids which were subsequently

concentrated along deep fracture systems which focused the migration of fluids along structures (Kerrich and Cassidy, 1994), such as the Santoy shear system.

## 5.2. Character and evolution of alteration and mineralization at Santoy and Fisher, Seabee Gold Operation

Analogous mineralogical relationships are present across lithologies from the Fisher property and Santoy Mine Complex alteration assemblages, spanning from the distal halo assemblage to the vein-adjacent calc-silicate assemblage (Fig. 12). Additionally, comparable alteration assemblage and mineralization characteristics at Fisher and Santoy suggests a closely related, multi-stage gold mineralizing system along the Santoy shear system.

Multiple lines of evidence presented in this study suggests that gold was introduced early into the system. An early inclusion-rich, intrusion-hosted  $Py_{1b}$  phase was identified to have formed prior to  $D_3$  and, as it is deformed and fractured, may have formed earlier (Fig. 12A). The characteristics and nature of occurrence of intrusion-hosted  $Py_{1b}$  are consistent with a magmatic-hydrothermal fluid origin and include the (i) greater proportion of inclusions, including minor gold inclusions; (ii) isolated occurrence in intrusive units; (iii) Co-Ni-Cu-Zn-As-Pb lattice-controlled and inclusion-controlled As-Ag-Te-W-Au-Bi trace-element signature (Beaudin et al., in review); and (iv) early paragenetic relationship with subsequent phases (Fig. 12A; e.g., Sillitoe and Thompson, 1998, Ispolatov et al., 2008, Mériaud and Jébrak, 2017, Mathieu, 2019). These characteristics along with the more fractured and deformed nature of  $Py_{1b}$ , suggest early gold and metal introduction into the system semi-coeval with intrusion formation pre- $D_1$ . The Hemlo deposit in the Superior province provides an example of a multi-stage hydrothermal system involving magmatic  $\pm$  metamorphic fluids that generated a calc-silicate alteration assemblage (Pan and Fleet, 1992, Muir, 2002, Tomkins et al., 2004). Early relict, subhedral-cubic or euhedral-colloform  $Py_{1a}$  was recognized within schists and is interpreted to have formed pre- to early-*syn*- $D_3$ , and at the same time as the highly deformed  $V_1$  veins (Fig. 12B). This phase suggests the presence of a pyrite supersaturated fluid early in the system and is a well-documented pyrite texture in magmatic-hydrothermal deposits (Barrie et al., 2009, Atanassova, 2010, Shang et al., 2016). In contrast the (i) isolated occurrence of colloform  $Py_{1a}$  adjacent to  $V_{2a}$  veins that cut schists semi-concordant to  $S_3$  foliation; (ii) a similar paragenetic relationship with adjacent distal halo to proximal alteration assemblages associated with subsequent Py phases; and (iii) a Co-Ni-W  $\pm$  Au-As-Ag-Cs-Te-Bi element signature, weakly similar but distinct from subsequent phases (Beaudin et al., in review), suggests an origin and relative time of formation semi-analogous with  $Py_{2a}$  and  $Py_{2b}$  (Fig. 12B). As such, this phase reveals the potential for early orogenic-style gold mineralization during late- $D_2$  to early-*syn*- $D_3$  deformation. These phases and proposed associated alteration assemblages were overprinted during subsequent main-stage alteration and sulfide-gold mineralization during *syn*-late- $D_3$  mineralization and late  $D_3$  remobilization.

In subsequent sulfide phases, comparable textures and mineralogical relationships are present across alteration assemblages from the Fisher property and Santoy Mine Complex (Fig. 12C–F). *Syn*-late- $D_3$  cyclical fluxes during main-stage mineralization developed (i) distal sericite-biotite-chlorite-clinozoisite  $\pm$  albite, titanite halo to vein-adjacent, coarse-grained diopside-K-feldspar-albite-actinolite  $\pm$  apatite, titanite calc-silicate alteration; (ii) thin, deformed quartz-albite  $\pm$  diopside-sulfide-K-feldspar-carbonate veins ( $V_{2a}$ ) and large, recrystallized quartz  $\pm$  sulfide veins ( $V_{2b}$ ); and (iii) main-stage  $Py_{2a, 2b}$ -Cpy $_2$ -Po $_1$ -Au mineralization, associated with native gold (Fig. 12C, D). Continuous late- $D_3$  deformation caused the calc-silicate alteration assemblage to be subsequently fractured and boudinaged, forming low pressure zones in which remobilized fracture-filling native gold and  $Py_3$ -Po $_2$ -Cpy $_3$ -Au-BiTel would preferentially precipitate (Fig. 12E, F). Similarly, during this stage Po $_2$  replacement of earlier Py phases is more evident in Santoy host

rocks, which is associated with an increase in gold mineralization (Fig. 12F). The characteristics, relative timing, and association with free gold identified for inclusion-rich  $Py_{2a}$ , overprinting cubic  $Py_{2b}$ , fracture-filling  $Py_3$ , and associated phases are typical of other orogenic gold deposits (e.g., Groves et al., 1998, Liu et al., 2011, Belousov et al., 2016, Gao et al., 2019). Additionally, a trace element study on these pyrite phases (Beaudin et al., in review) identified As-Ag-Te-Bi-Au and variable Co-Ni-Cu  $\pm$  Se-Sb-W element signatures in  $Py_{1a, 2a, 2b, 3}$ , characteristic of orogenically-derived fluids (e.g., Belousov et al., 2016, Gao et al., 2019). As such, the similarities between sulfide phases and associated alteration likely reflect *syn*-late  $D_3$  main-stage mineralization (Fig. 12C, D) and subsequent late  $D_3$  remobilization (Fig. 12E, F), respectively, from hydrothermal fluids that propagated along the Santoy shear system during regional orogenesis.

The most significant difference in the mineralization between the Santoy Mine Complex and Fisher property is the increase in modal Po and associated gold at Santoy (Fig. 12D, F). This discrepancy between Po-Au abundance between Fisher and Santoy could be related to an increase in fluid fluxes and higher degree of remobilization present at Santoy. This difference is likely structurally influenced, where the compressional jog formed by the buttressing Packman Lake pluton facilitated fluid flow and preferentially developed and locally remobilized gold during  $D_3$  (Cox et al., 2001, Wood, 2016). Similarly, shearing within the tighter section of the corridor at Fisher between the Eisler intrusive suite and the Uskik granodiorite, potentially produced finer-grained fabrics and less preferential low pressure structural conditions. Lower pore fluid pressure, higher porosity, and space for mineral growth throughout  $D_3$  deformation could have promoted a higher degree of Po replacement of Py at Santoy (Fig. 12D, F; Cox et al., 2001). This notion is further supported by the increase in Sp, Cpy, Gn, and other base metals in  $V_{2b}$  veins that cut intrusive lithologies, suggesting a higher degree of remobilization and scavenging of metals from juxtaposed host rocks during large pressure drops (Sibson et al., 1988). It is important to note that the absence of hematitization and significant potassic alteration in  $V_{2b}$  veins that cut intrusive lithologies, as well as similar alteration of vein-hosted wall rock fragments across lithologies, indicate that  $V_{2b}$  are likely not of magmatic-hydrothermal origin and are interpreted to be associated with main-stage mineralization during *syn*-late- $D_3$ . In summary, the consistency observed across the sulfide mineral phases, mineralization characteristics, and mineralogical association with gold suggests a closely related, multi-stage gold mineralizing system along the Santoy shear system, from Santoy to Fisher. Previous studies (e.g., Tourigny 2003b, Tourigny et al., 2004, McEwan, 2013, Wood, 2016, Onstad, 2021) have suggested an orogenic model for the Seabee Gold Operation, including the Seabee and Santoy mine complexes, as well as the Fisher property. Furthermore, these proposed models for the nature of mineralization along the Santoy shear system are supported in this study by the elemental variation and mineralogical trend present in alteration mineral phases associated with progressive mineralization. The petrographic analysis on sulfide mineral phases in this study and concurrent trace-element analyses (Beaudin et al., in review) suggest a complex, albeit interconnected, multi-stage, dominantly orogenic mineralizing system along the Santoy shear system, with minor early gold enrichment.

## 6. Conclusions

Host rocks at the Santoy Mine Complex and Fisher property of the Seabee Gold Operation portray characteristics indicative of an interconnected, dominantly orogenic-style gold mineralizing system within a greenschist- to lower amphibolite-grade, Paleoproterozoic greenstone belt. The meta-basalt to Hbl-Bt-Chl schists and host rocks at Fisher and Santoy show similar distal Ser-Bt-Chl-Czo  $\pm$  Ab-Ttn halo and vein-adjacent, coarse-grained Di-Kfs-Ab-Act  $\pm$  Ap-Ttn calc-silicate alteration associated with foliation parallel Py-Po-Cpy  $\pm$  Au-Mt and fracture-filling Py-Po-Cpy  $\pm$  Au-BiTel-Mt-Gn-Sp mineralization, respectively.

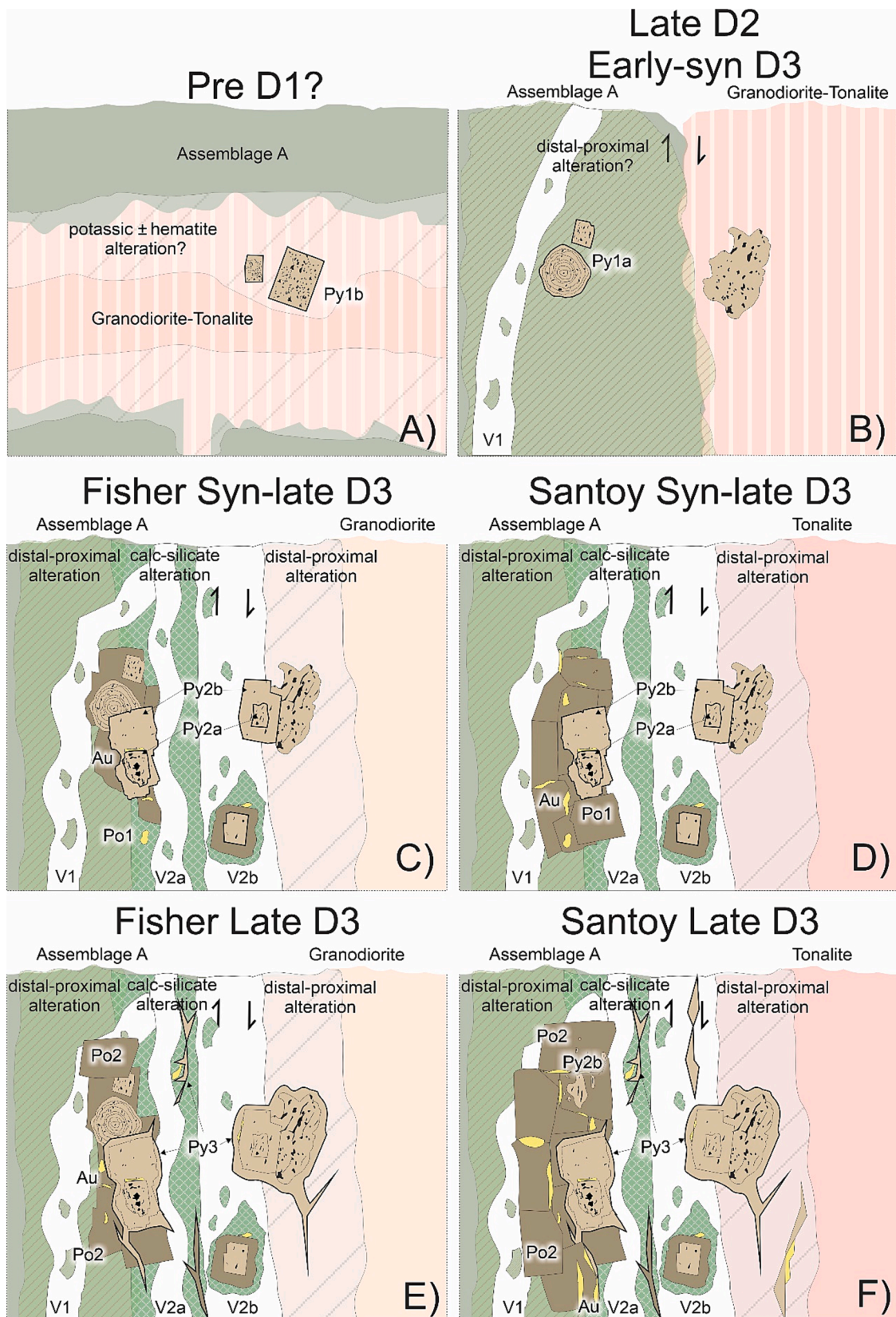


**Fig. 12.** Schematic sections highlighting the characteristics, mineralogical relationships, and relative timing of alteration and mineralization between the Fisher property and Santoy Mine Complex. (A) pre-D<sub>1</sub> Py<sub>1b</sub> mineralization and associated proposed alteration assemblage. (B) Rotation of stratigraphy from orogenesis and development of shear zones, late-D<sub>2</sub> to early-syn-D<sub>3</sub> Py<sub>1a</sub> mineralization, proposed V<sub>1</sub> vein generation, and associated distal halo to proximal alteration. (C–D) Syn-late D<sub>3</sub> main-stage Py<sub>2a</sub>-Py<sub>2b</sub>-Po<sub>1</sub>-Au mineralization, V<sub>2a</sub> and V<sub>2b</sub> vein generation, and associated distal halo to vein-adjacent calc-silicate alteration at (C) Fisher and (D) Santoy, with an increase in Po<sub>1</sub> and Au. (E–F) late D<sub>3</sub> remobilization and Py<sub>2</sub>-Po<sub>2</sub>-Au mineralization at (E) Fisher and (F) Santoy, with an increase in Po<sub>2</sub> and Au.

These alteration characteristics are similar in intrusive lithologies. The rocks at Santoy and Fisher are also cut by similar quartz vein generations (V<sub>1</sub>-V<sub>3</sub>). Together the comparable mineralogy, textures, vein generations, and alteration assemblages between Fisher and Santoy suggest an interconnected relationship between lithology, structures, hydrothermal processes and associated alteration and mineralization. This is further supported by the corresponding trends shown by Fisher and Santoy Fsp, Am, Chl, and Bt alteration mineral chemistry which yield geothermobarometric constraints (~320–330 °C, 3 kbar, ~9 km depth) typical of orogenic gold systems.

In relation to the evolution of the Trans-Hudson orogen, the main-stage alteration (distal halo to vein adjacent) and associated sulfide-gold mineralization (Py<sub>2a,2b</sub>-Cpy<sub>2</sub>-Po<sub>2</sub>-Au) primarily commenced *syn*-late-D<sub>3</sub> concurrent with late- to post- collisional deformation present throughout the Reindeer zone. Continuous deformation (late-D<sub>3</sub>; ca. 1755 Ma) however, resulted in the remobilization of sulfide minerals and gold (Py<sub>3</sub>-Po<sub>2</sub>-Cpy<sub>3</sub>-Au-BiTeI) within fractures and low-pressure zones, potentially being mobilized and upgraded to a higher degree at Santoy by cyclical fluid fluxes and preferential precipitation within a higher density of fractures. Early pyrite phases identified in this study, however, provides new constraints towards the mineralizing system at the Santoy Mine Complex and Fisher property at the Seabee Gold Operation. Early, intrusion-hosted Py<sub>1b</sub> and colloform Py<sub>1a</sub>, the former of which yields a magmatic-hydrothermal origin, suggests an early introduction of gold into the system semi-concurrent with intrusions (magmatic-hydrothermal; pre-D<sub>1</sub>) and during the onset of gold mineralization (orogenic; *syn*-D<sub>3</sub>), respectively. Overall, the nature of mineralization at the Santoy Mine Complex and Fisher property at the Seabee Gold operation portrays textural, mineralogical, and mineralization typical of an interconnected multi-stage orogenic gold mineralizing system, with potential for a minor introduction of gold into the mineralizing system prior to or during orogenesis, providing implications for future exploration in the Glennie domain. As such, this study emphasizes the importance of considering the tectonic and magmatic evolution of an orogenic terrane as an integral part of delineating multi-stage ore genesis and upgrading.

#### CRedit authorship contribution statement

**D. Beaudin:** Formal analysis, Investigation, Resources, Validation, Writing – original draft, Writing – review & editing. **C.A. Partin:** Conceptualization, Investigation, Methodology, Project administration, Resources, Supervision, Validation, Visualization, Writing – original draft, Writing – review & editing. **K. Ansdell:** Conceptualization, Investigation, Methodology, Project administration, Resources, Supervision, Validation, Visualization, Writing – original draft, Writing – review & editing. **P. Yang:** Investigation, Validation.

#### Declaration of competing interest

The authors declare that they have no known competing financial interests or personal relationships that could have appeared to influence the work reported in this paper.

#### Data availability

I have shared the link to my data at the attach file stage

#### Acknowledgments

This research was funded by a Natural Sciences and Engineering Research Council of Canada Alliance grant (grant ALLRP 555177 – 20 to K.A. and C.A.P.) and a Natural Sciences and Engineering Research Council – Canada Graduate Scholarships – Masters (to D.B.). This paper forms part of a MSc thesis at the University of Saskatchewan by D.B. Anders Carlson, Paul Kremer, Devon Stuebing, and others at SSR Mining

Inc. are thanked for their expertise and access to the resources pertinent to this research. Two anonymous reviewers are thanked for their constructive comments that improved the manuscript.

#### Appendix A. Supplementary data

Supplementary data to this article can be found online at <https://doi.org/10.1016/j.oregeorev.2024.105950>.

#### References

- Ansdell, K.M., 2005. Tectonic evolution of the Manitoba-Saskatchewan segment of the Paleoproterozoic Trans-Hudson Orogen, Canada. *Can. J. Earth Sci.* 42, 741–759. <https://doi.org/10.1139/e05-035>.
- Ansdell, K.M., Kyser, T.K., 1992. Mesothermal Gold Mineralization in a Proterozoic Greenstone Belt: Western Flin Flon Domain, Saskatchewan, Canada. *Econ. Geol.* 87, 1496–1524.
- Ansdell, K.M., Lucas, S.B., Connors, K., Stern, R.A., 1995. Kisseynew metasedimentary gneiss belt, Trans-Hudson orogen (Canada): Back-arc origin and collisional inversion. *Geology* 23, 1039–1043. [https://doi.org/10.1130/0091-7613\(1995\)023<1039:KMGBTH>2.3.CO;2](https://doi.org/10.1130/0091-7613(1995)023<1039:KMGBTH>2.3.CO;2).
- Asbury, B.C., 1986. The Komis gold deposit and EP zone, Waddy Lake area, Saskatchewan. In: Clark, L.A. (Eds.) Gold in the Western Shield, Canadian Institute of Mining and Metallurgy, Special Volume 38, pp. 221–228.
- Ashton, K.E., Lewry, J.F., Heaman, L.M., Hartlaub, R.P., Stauffer, M.R., Tran, H.T., 2005. The Pelican Thrust Zone: Basal detachment between the Archean Sask Craton and Paleoproterozoic Flin Flon - Glennie Complex, western Trans-Hudson Orogen. *Can. J. Earth Sci.* 42, 685–706. <https://doi.org/10.1139/e04-035>.
- Ashton, K.E., 1999. A proposed lithotectonic domain re-classification of the southeastern Reindeer Zone in Saskatchewan; In Summary of Investigations 1999, Volume 1, Saskatchewan Geological Survey, Saskatchewan Energy Mines, Miscellaneous Report 99-4.1, pp. 92–100.
- Atanassova, R., 2010. Environmental significance of pyrite with colloform textures. *Comptes Rendus De L'academie Bulgare Des Sciences*, p. 63.
- Barrie, C.D., Boyce, A.J., Boyle, A.P., Williams, P.J., Blake, K., Ogawara, T., Akai, J., Prior, D.J., 2009. Growth controls in colloform pyrite. *Am. Mineral.* 94 (4), 415–429.
- Basnett, R., 1999. Seabee Mine. In: Ashton, K. E. and Harper, C. T. (Eds.), MinExpo'96 symposium; Advances in Saskatchewan Geology and Mineral Deposits, Saskatchewan Geological Society, Special Publication 14, pp. 72–80.
- Belousov, I., Large, R.R., Meffre, S., Danyushevsky, L.V., Steadman, J., Beardsmore, T., 2016. Pyrite compositions from VHMS and orogenic Au deposits in the Yilgarn Craton. *Ore Geol. Rev.* 79, 474–499.
- Beaudin, D., Partin, C.A., Ansdell, K. Voinot, A., Creaser, R., Ickert, R., In review. Multi-stage orogenic gold-mineralizing systematics at the Seabee Gold Operation, northern Saskatchewan, Canada: Constraints from pyrite chemistry and geochronology, *Mineralium Deposita*.
- Bickford, M.E., Van Schmus, W.R., Collerson, K.D., Macdonald, R., 1987. U-Pb zircon geochronology project: new results and interpretations. In: Summary of Investigations 1987, Saskatchewan Geological Survey, Saskatchewan Energy Mines, Miscellaneous Report. 87-4, pp. 76–79.
- Bucci, L.A., McNaughton, N.J., Fletcher, I.R., Groves, D.I., Kositcin, N., Stein, H.J., Hagemann, S.G., 2004. Timing and duration of high-temperature gold mineralization and spatially associated granitoid magmatism at Chalice, Yilgarn Craton, Western Australia. *Econ. Geol.* 99, 1123–1144. <https://doi.org/10.2113/gsecongeo.99.6.1123>.
- Cathelineau, M., 1988. Cation site occupancy in chlorites and illites as a function of temperature. *Clay Miner.* 23, 471–485. <https://doi.org/10.1180/claymin.1988.023.4.13>.
- Chantler, C.T., 2000. Detailed tabulation of atomic form factors, photoelectric absorption and scattering cross section, and mass attenuation coefficients in the vicinity of absorption edges in the soft x-ray (Z=30-36, Z=60-89, E=0.1 keV-10keV), addressing convergence issues of earlier work. *J. Phys. Chem. Ref. Data* 29 (4), 597–1048.
- Chiarenzelli, J.R., 1989. The Nistowiak and Guncoat Gneisses: implications for the tectonics of the Glennie and La Ronge domains. Unpublished PhD thesis. University of Kansas, Northern Saskatchewan, Canada, p. 229.
- Corrigan, D., Hajnal, Z., Németh, B., Lucas, S.B., 2005. Tectonic framework of a Paleoproterozoic arc-continent to continent-continent collisional zone, Trans-Hudson Orogen, from geological and seismic reflection studies. *Can. J. Earth Sci.* 42, 421–434. <https://doi.org/10.1139/e05-025>.
- Cook, N.J., Ciobanu, C.L., 2004. Bismuth tellurides and sulphosalts from the Larga hydrothermal system, Metaliferi Mts, Romania: Paragenesis and genetic significance. *Mineral. Mag.* 68 (2), 301–321. <https://doi.org/10.1180/0026461046820188>.
- Corrigan, D., Galley, A., Pehrsson, S., 2007. Tectonic evolution and metallogeny of the southwestern Trans-Hudson Orogen. In: Goodfellow, W.D. (Ed.), *Mineral Deposits of Canada: A Synthesis of Major Deposit-Types, District Metallogeny, the Evolution of Geological Provinces, and Exploration Methods*. Geological Association of Canada, Mineral Deposits Division, Special Publication N.
- Corrigan, D., Pehrsson, S., Wodicka, N., de Kemp, E., 2009. The Palaeoproterozoic Trans-Hudson Orogen: A prototype of modern accretionary processes. In: *Ancient orogens and modern analogues*. Geological Society (of London) Special Publications 327, pp. 457–479. <https://doi.org/10.1144/SP327.19>.

- Cox, S.F., 1999. Deformational controls on the dynamics of fluid flow in mesothermal gold systems. *Geochem. Soc. Spec. Publ.* 155, 123–140. <https://doi.org/10.1144/GSL.SP.1999.155.01.10>.
- Cox, S.F., Knackstedt, M.A., Braun, J., 2001. Principles of Structural Control on Permeability and Fluid Flow in Hydrothermal Systems. In: Richards, J.P., Tosdal, R. M. (Eds.), *Structural Controls on Ore Genesis* 14. Society of Economic Geologists, pp. 1–24. <https://doi.org/10.5382/Rev.14.01>.
- Deer, W.A., Howie, R.A., Zussman, J., 1998. Rock-forming minerals, volume 2B (second edition): double-chain silicates. In *Rock-forming minerals, volume 2B (second edition): double-chain silicates*.
- de Souza, S.R.C., Botelho, N.F., Jiménez, F.A.C., Dantas, E.L., Reis, M.A., Viana, C.S., 2021. Mineralization and hydrothermal alteration in the Mamão orogenic gold deposit, Andorinhas greenstone belt, Carajás Province, Brazil. *J. S. Am. Earth Sci.* 112 <https://doi.org/10.1016/j.jsames.2021.103548>.
- De Souza, S., Dubé, B., Mercier-Langevin, P., McNicoll, V., Dupuis, C., Kjarsgaard, I., 2019. Hydrothermal alteration mineralogy and geochemistry of the Archean world-class Canadian malartic disseminated-stockwork gold deposit, southern Abitibi Greenstone Belt, Quebec, Canada. *Econ. Geol.* 114, 1057–1094. <https://doi.org/10.5382/econgeo.4674>.
- Delaney, G.D., Cutler, S.A., 1992. Geological Setting of the “Santoy Lake” Gold Camp (Part of NTS 63M-11 and -12). In: Summary of Investigations 1992, Saskatchewan Geological Survey, Saskatchewan Energy Mines, Misc. Rep. 92-4, pp. 30–40.
- Delaney, G.D., 1986. Bedrock Geological Mapping, Laonil Lake Area (Part of NTS 63M-11 and -12). In: Summary of investigations 1986, Saskatchewan Geological Survey, Ministry of Energy and Resources, Miscellaneous Report 86-4, pp. 8–17.
- Delaney, G.D., 1992. Gold in the Glennie Domain. In: Saskatchewan Geological Survey, Saskatchewan Energy and Mines, Miscellaneous Report 92-5. p. 75. Saskatchewan Energy and Mines. Mineral Development Branch, Regina.
- Delaney, G.D., 2016. Geology of the Pine Lake Greenstone Belt, Laonil-Uskik Lakes Area (Parts of NTS63M-11 and 12). In: Saskatchewan Geological Survey, Ministry on the Economy, Geoscience Map 2016-1, 1:50000 scale map.
- Dubé, B., Mercier-Langevin, P., 2015. Targeted Geoscience Initiative 4: Contributions to the understanding of Precambrian lode gold deposits and implications for exploration. Geological Survey of Canada, Open File 7852, p. 293.
- Durocher, K.E., 1997. A study of the P-T-t-fluid evolution of the Glennie domain, Trans-Hudson Orogen. Unpublished PhD thesis. University of Saskatchewan, p. 302.
- Durocher, K.E., Cutler, S.A., Delaney, G.D., Kyser, T.K., 1992. Gold Occurrences in the “Santoy Lake” Area, Glennie Domain, Trans-Hudson Orogen. In: Summary of Investigations 1992, Saskatchewan Geological Survey, Saskatchewan Energy Mines, Miscellaneous Report 92-4, pp. 41–50.
- Durocher, K.E., Kyser, T.K., Delaney, G.D., 2001. Thermotectonic studies in the paleoproterozoic glennie domain, trans-hudson orogen, Canada. *Precamb. Res.* 109, 175–202. [https://doi.org/10.1016/S0301-9268\(01\)00144-9](https://doi.org/10.1016/S0301-9268(01)00144-9).
- Elliott, C.G., 1995. The Tabernor fault and Proterozoic and Phanerozoic movements in Saskatchewan and Manitoba. In: LITHOPROBE Trans-Hudson Orogen Transect, 5th Transect Meeting, LITHOPROBE Secret, University of British Columbia, Report 48, pp. 148–155.
- Fedorowich, J.S., Kerrich, R., Stauffer, M.R., 1995. Geodynamic evolution and thermal history of the central Flin Flon Domain, Trans-Hudson Orogen: Constraints from structural development, 40Ar/39Ar, and stable isotope geothermometry. *Tectonics* 14 (2), 472–503.
- Fumerton, S.L., Stauffer, M.R., Lewry, J.F., 1984. The Wathaman batholith: largest known Precambrian pluton. *Can. J. Earth Sci.* 21, 1082–1097. <https://doi.org/10.1139/e84-113>.
- GabroSoft, 2011. Spreadsheets for atoms per formula unit calculations. Available at [gabrosoft.org](http://gabrosoft.org).
- Gaillard, N., Williams-Jones, A.E., Clark, J.R., Lypaczewski, P., Salvi, S., Perrouty, S., Piette-Lauzière, N., Guilmette, C., Linnen, R.L., 2018. Mica composition as a vector to gold mineralization: Deciphering hydrothermal and metamorphic effects in the Malartic district, Quebec. *Ore Geol. Rev.* 95, 789–820. <https://doi.org/10.1016/j.oregeorev.2018.02.009>.
- Gao, F., Du, Y., Pang, Z., Du, Y., Xin, F., Xie, J., 2019. LA-ICP-MS trace-element analysis of pyrite from the huanxiangwa gold deposit, xiong'er shan district, china: Implications for ore genesis. *Minerals* 9, 1–15. <https://doi.org/10.3390/min9030157>.
- Goldfarb, R.J., Baker, T., Dubé, B., Groves, D.I., Hart, C.J.R., Gosselin, P., 2005. Distribution, Character, and Genesis of Gold Deposits in Metamorphic Terranes. *Econ. Geol.* 100th Anniversary 100, 407–450.
- Goldfarb, R.J., Groves, D.I., 2015. Orogenic gold: Common or evolving fluid and metal sources through time. *Lithos* 233, 2–26. <https://doi.org/10.1016/j.lithos.2015.07.011>.
- Groves, D.I., 1993. The crustal continuum model for late-Archaean lode-gold deposits of the Yilgarn Block, Western Australia. *Miner. Deposita* 28, 366–374. <https://doi.org/10.1007/BF02431596>.
- Groves, D.I., Goldfarb, R.J., Gebre-Mariam, M., Hagemann, S.G., Robert, F., 1998. Orogenic gold deposits: a proposed classification in the context of their crustal distribution and relationship to other gold deposit types. *Ore Geol. Rev.* 13, 7–27. [https://doi.org/10.1016/S0169-1368\(97\)00012-7](https://doi.org/10.1016/S0169-1368(97)00012-7).
- Groves, D.I., Santosh, M., Goldfarb, R.J., Zhang, L., 2018. Structural geometry of orogenic gold deposits: Implications for exploration of world-class and giant deposits. *Geosci. Front.* 9, 1163–1177. <https://doi.org/10.1016/j.gsf.2018.01.006>.
- Groves, D.I., Santosh, M., Deng, J., Wang, Q., Yang, L., Zhang, L., 2020. A holistic model for the origin of orogenic gold deposits and its implications for exploration. *Miner. Deposita* 55, 275–292. <https://doi.org/10.1007/s00126-019-00877-5>.
- Helmstaedt, H., 1986. Report on the geology and structure of the Seabee and Currie Rose properties, Laonil Lake, Saskatchewan. In: Internal Report, Placer Development Ltd., p. 714.
- Hoffman, P.F., 1988. United plates of America, the birth of a craton: Early Proterozoic assembly and growth of Laurentia. *Annu. Rev. Earth Planet. Sci.* 16, 543–603. <https://doi.org/10.1146/annurev.ea.16.050188.002551>.
- Hrdy, F., Kyser, T.K., 1995. Origin, timing, and fluid characteristics of an auriferous event: the Proterozoic Jasper lode gold deposit, Saskatchewan, Canada. *Econ. Geol.* 90, 1918–1933. <https://doi.org/10.2113/gsecongeo.90.7.1918>.
- Ispolatov, V., Lafrance, B., Dubé, B., Creaser, R., Hamilton, M., 2008. Geologic and structural setting of gold mineralization in the Kirkland Lake-Larder Lake gold belt, Ontario. *Econ. Geol.* 103, 1309–1340. <https://doi.org/10.2113/gsecongeo.103.6.1309>.
- Kenwood, S., 2017. NI 43-101 Technical Report, Fisher Property. In: Internal Report, SSR Mining Ltd., p. 51.
- Kerrich, R., Cassidy, K.F., 1994. Temporal relationships of lode gold mineralization to accretion, magmatism, metamorphism and deformation - Archean to present: A review. *Ore Geol. Rev.* 9, 263–310. [https://doi.org/10.1016/0169-1368\(94\)90001-9](https://doi.org/10.1016/0169-1368(94)90001-9).
- Kranidiotis, P., MacLean, W.H., 1987. Systematics of chlorite alteration at the Phelps Dodge massive sulfide deposit, Matagami, Quebec. *Econ. Geol.* 82, 1898–1911. <https://doi.org/10.2113/gsecongeo.82.7.1898>.
- Lafrance, B., 1999. Gold Studies in the Byers Fault-Waddy Lake Area, La-Ronge Domain. In: Summary of Investigations 1999, Volume 2, Saskatchewan Geological Survey, Saskatchewan Energy and Mines, Miscellaneous Report 99-4.2, pp. 202–207.
- Lafrance, B., 2000. The Round Lake Stock: A Structural Trap for the Emplacement of the Fracture-controlled Komis Gold Deposit in the La Ronge Domain, Northern Saskatchewan. In: Summary of Investigations 2000, Volume 2, Saskatchewan Geological Survey, Saskatchewan Energy and Mines, Miscellaneous Report 2000-4.2, pp. 74–78.
- Lawley, C.J.M., Yang, X.M., Selby, D., Davis, W., Zhang, S., Petts, D.C., Jackson, S.E., 2020. Sedimentary basin controls on orogenic gold deposits: New constraints from U-Pb detrital zircon and Re-Os sulphide geochronology, Lynn Lake greenstone belt, Canada. *Ore Geol. Rev.* 126, 103790.
- Leake, B.E., Woolley, A.R., Arps, C.E.S., Birch, W.D., Gilbert, M.C., Grice, J.D., Hawthorne, F.C., Kato, A., Kisch, H.J., Krivovichev, V.G., Linthout, K., Laird, J., Mandarino, J.A., Maresch, W.V., Nickel, E.H., Rock, N.M.S., Schumacher, J.C., Smith, D.C., Stephenson, N.C.N., Ungaretti, L., Whittaker, E.J.W., Youzhi, G., 1997. Nomenclature of amphiboles: Report of the subcommittee on amphiboles of the international mineralogical association, submission on new minerals and mineral names. *Am. Mineral.* 82, 1019–1037. <https://doi.org/10.1180/minmag.1997.061.405.13>.
- Lewry, J.F., Collerson, K.D., 1990. The Trans-Hudson Orogen: extent, subdivisions and problems. In: Lewry, J.F., Stauffer, M.R. (Eds.) *The Early Proterozoic Trans-Hudson Orogen of North America*. Geological Association of Canada, Special Paper 37, pp. 35–41.
- Lewry, J.F., Thomas, D.J., Macdonald, R., Chiarenzelli, J., 1990. Structural relations in accreted terranes of the Trans-Hudson Orogen, Saskatchewan: telescoping in a collisional regime? In: Lewry, J.F. and Stauffer, M.R. (eds.), *The Early Proterozoic Trans-Hudson Orogen of North America*, Geological Association of Canada, Special Paper 37, pp. 75–94.
- Lewry, J.F., Hajnal, Z., Green, A., Lucas, S.B., White, D., Stauffer, M.R., Ashton, K.E., Weber, W., Clowes, R., 1994. Structure of a Paleoproterozoic continent-continent collision zone: a LITHOPROBE seismic reflection profile across the Trans-Hudson Orogen, Canada. *Tectonophysics* 232, 143–160. [https://doi.org/10.1016/0040-1951\(94\)90081-7](https://doi.org/10.1016/0040-1951(94)90081-7).
- Lewry, J.F., 1977. The Geology of the Glennie Lake Area. In: Saskatchewan Department of Mineral Resources, Report 143, pp. 1–59.
- Li, X., Zhang, C., Behrens, H., Holtz, F., 2020. Calculating biotite formula from electron microprobe analysis data using a machine learning method based on principal components regression. *Lithos* 356–357, 105371.
- Liu, Y., Chi, G., Bethune, K.M., Dubé, B., 2011. Fluid dynamics and fluid-structural relationships in the Red Lake mine trend, Red Lake greenstone belt, Ontario, Canada. *Geofluids* 11, 260–279. <https://doi.org/10.1111/j.1468-8123.2011.00336.x>.
- Lucas, S.B., Stern, R.A., Syme, E.C., Reilly, B.A., Thomas, D.J., 1996. Intraoceanic tectonics and the development of continental crust: 1.92–1.84 Ga evolution of the Flin Flon Belt, Canada. *Bull. Geol. Soc. Am.* 108, 602–629. [https://doi.org/10.1130/0016-7606\(1996\)108<0602:ITATDO>2.3.CO;2](https://doi.org/10.1130/0016-7606(1996)108<0602:ITATDO>2.3.CO;2).
- Mathieu, L., 2019. Detecting magmatic-derived fluids using pyrite chemistry: Example of the Chibougamau area, Abitibi Subprovince, Québec. *Ore Geol. Rev.* 114, 1–20. <https://doi.org/10.1016/j.oregeorev.2019.103127>.
- Maxeiner, R.O., Kamber, B.S., 2011. La Ronge ‘Horseshoe’ Project : Bedrock Geology of the Hebden Lake Area at the Transition Between the Western Glennie Domain and Southern Kisseynew and La Ronge Domains (parts of NTS 73P / 07); in Summary of Investigations 2011, Volume 2. In: Saskatchewan Geological Survey, Ministry of Energy and Resources, Miscellaneous Report.
- McCuaig, T.C., Kerrich, R., 1998. P-T-t-deformation-fluid characteristics of lode gold deposits: Evidence from alteration systematics. *Ore Geol. Rev.* [https://doi.org/10.1016/S0169-1368\(98\)00010-9](https://doi.org/10.1016/S0169-1368(98)00010-9).
- McEwan, B., 2013. Summary of Geological Mapping of the Santoy Mine Area during the Summer of 2012. In: Internal Report. Claude Resources Inc., p. 24.
- McNicoll, V.J., Delaney, G.D., Parrish, R.R., Heaman, Larry, M., 1992. U-Pb age determinations from the Glennie Lake Domain, Trans-Hudson Orogen, Saskatchewan. In: Radiogenic Age and Isotopic Studies, Report 6, Geological Survey of Canada, paper 92-2, pp. 57–72.

- Meffre, S., Large, R.R., Steadman, J.A., Gregory, D.D., Stepanov, A.S., Kamenetsky, V.S., Ehrig, K., Scott, R.J., 2016. Multi-stage enrichment processes for large gold-bearing ore deposits. *Ore Geol. Rev.* 76, 268–279. <https://doi.org/10.1016/j.oregeorev.2015.09.002>.
- Mériaud, N., Jébrak, M., 2017. From intrusion-related to orogenic mineralization: The Wasamac deposit, Abitibi Greenstone Belt, Canada. *Ore Geol. Rev.* 84, 289–308. <https://doi.org/10.1016/j.oregeorev.2017.01.021>.
- Meyer, M.T., Bickford, M.E., Lewry, J.F., 1992. The Wathaman Batholith: an early Proterozoic continental arc in the Trans-Hudson Orogenic Belt, Canada. *Geol. Soc. Am. Bull.* 104, 1073–1085. [https://doi.org/10.1130/0016-7606\(1992\)104<1073:TWBAEP>2.3.CO;2](https://doi.org/10.1130/0016-7606(1992)104<1073:TWBAEP>2.3.CO;2).
- Morelli, R.M., MacLachlan, K., 2012. Saskatchewan Gold : Mineralization Styles and Mining History. In Saskatchewan Ministry of Energy and Resources, Report 262, p. 171.
- Morimoto, N., 1988. Nomenclature of Pyroxenes. *Mineral. Petrol.* 39 (1), 55–76. <https://doi.org/10.1007/BF01226262>.
- Mueller, A.G., 1992. Petrogenesis of amphibole-biotite-calcite-plagioclase alteration and laminated gold-silver quartz veins in four Archean shear zones of the Norseman district, Western Australia. *Can. J. Earth Sci.* 29, 388–417. <https://doi.org/10.1139/e92-036>.
- Muir, T.L., 2002. The Hemlo gold deposit, Ontario, Canada: principal deposit characteristics and constraints on mineralization. *Ore Geol. Rev.* 21 (1–2), 1–66. [https://doi.org/10.1016/S0169-1368\(02\)00066-5](https://doi.org/10.1016/S0169-1368(02)00066-5).
- Ojala, V.J., Ridley, J.R., Groves, D.I., Hall, G.C., 1993. The Granny Smith gold deposit: the role of heterogeneous stress distribution at an irregular granitoid contact in a greenschist facies terrane. *Miner. Deposita* 28, 409–419. <https://doi.org/10.1007/BF02431599>.
- Onstad, C., 2021. *Geology, Petrography, and Geochemistry of Fisher Property Rocks and Their Altered Equivalents, and Relationship to Auriferous Quartz Veins, Glennie Domain*. Unpublished Msc Thesis. University of Saskatchewan, Northern Saskatchewan, p. 184.
- Pan, Y., Fleet, M.E., 1992. Calc-silicate alteration in the Hemlo gold deposit, Ontario: mineral assemblages, P-T-X constraints, and significance. *Econ. Geol.* 87, 1104–1120. <https://doi.org/10.2113/gsecongeo.87.4.1104>.
- Pouchou, J.L., Pichoir, F., 1984. New model for quantitative x-ray microanalysis. Part II: Application to in-depth analysis of heterogeneous samples. *Recherche Aerospaciale (English Edition)* 47–65.
- Ridley, J., Diamond, L.W., 2020. Fluid Chemistry of Orogenic Lode Gold Deposits and Implications for Genetic Models. In: *Gold in 2000*, pp. 141–162. <https://doi.org/10.5382/rev.13.04>.
- Robert, F., 2001. Syenite-associated disseminated gold deposits in the Abitibi greenstone belt, Canada. *Miner. Deposita* 36, 503–516. <https://doi.org/10.1007/s001260100186>.
- Samson, I.M., Blackburn, W.H., Gagnon, J.E., 1999. Paragenesis and composition of amphibole and biotite in the MacLellan gold deposit, Lynn Lake greenstone belt, Manitoba, Canada. *Can. Mineral.* 37, 1405–1421.
- Schneider, D.A., Heizler, M.T., Bickford, M.E., Wortman, G.L., Condie, K.C., Perilli, S., 2007. Timing constraints of orogeny to cratonization: Thermochronology of the Paleoproterozoic Trans-Hudson orogen, Manitoba and Saskatchewan, Canada. *Precamb. Res.* 153, 65–95. <https://doi.org/10.1016/j.precamres.2006.11.007>.
- Shang, G., Fei, H., Yinghui, W., Wenyuan, G., 2016. A Review of Research Progress in the Genesis of Colloform Pyrite and Its Environmental Indications. *Acta Geol. Sin. (English Edition)* 90, 1353–1369. <https://doi.org/10.1111/1755-6724.12774>.
- Sibson, R.H., Robert, F., Poulsen, K.H., 1988. High-angle reverse faults, fluid-pressure cycling, and mesothermal gold-quartz deposits. *Geology* 16, 551–555. [https://doi.org/10.1130/0091-7613\(1988\)016<0551:HARFFP>2.3.CO;2](https://doi.org/10.1130/0091-7613(1988)016<0551:HARFFP>2.3.CO;2).
- Sillitoe, R.H., Thompson, J.F.H., 1998. Intrusion-related vein gold deposits: Types, tectono-magmatic settings and difficulties of distinction from Orogenic Gold Deposits. *Resour. Geol.* 48, 237–250. <https://doi.org/10.1111/j.1751-3928.1998.tb00021.x>.
- Simpson, R.G., 2006. Technical report and mineral resource estimate, Tower East gold deposit, Greater Waddy Lake Project; NI 43-101. Report GBN, GeoSim Services Inc., p. 89.
- Srk Consulting, 2017. NI 43-101 Technical Report for the Seabee Gold Operation, Saskatchewan, Canada. [www.ssrmining.com/resources/2017-10-20-Seabee-Gold-Operation-Technical-Report](http://www.ssrmining.com/resources/2017-10-20-Seabee-Gold-Operation-Technical-Report), Srk Consulting, p. 127.
- Stauffer, M.R., 1984. Manikewan: An early proterozoic ocean in central Canada, its igneous history and orogenic closure. *Precamb. Res.* 25, 257–281. [https://doi.org/10.1016/0301-9268\(84\)90036-6](https://doi.org/10.1016/0301-9268(84)90036-6).
- Stern, R.A., Syme, E.C., Bailes, A.H., Lucas, S.B., 1995. Paleoproterozoic (1.90–1.86 Ga) arc volcanism in the Flin Flon Belt, Trans-Hudson Orogen, Canada. *Contrib. Mineral. Petrol.* 119, 117–141. <https://doi.org/10.1007/BF00307276>.
- Thomas, D.J., Heaman, L.M., 1994. Geologic setting of the Jolu gold mine, Saskatchewan: U-Pb age constraints on plutonism, deformation, mineralization, and metamorphism. *Econ. Geol.* 89, 1017–1029. <https://doi.org/10.2113/gsecongeo.89.5.1017>.
- Tomkins, A.G., Pattison, D.R.M., Zaleski, E., 2004. The Hemlo Gold Deposit, Ontario: An example of melting and mobilization of a precious metal-sulfosalt assemblage during amphibolite facies metamorphism and deformation. *Econ. Geol.* 99, 1063–1084. <https://doi.org/10.2113/gsecongeo.99.6.1063>.
- Tourigny, G., Chi, G., Yuhasz, C., Olson, R., Berger, J., Soloman, J., 2004. Structural controls and temperature-pressure conditions of gold-bearing quartz vein systems at the Seabee mine, northern Saskatchewan. In: *Summary of Investigations 2004, Volume 2, Saskatchewan Geological Survey, Saskatchewan Industry Resources, Miscellaneous Report 2004-4.2, Paper A-2*, p. 18.
- Tourigny, G., 2003a. Detailed Study of the Bingo North and Bingo South Gold Showings, Dickens Lake Area, La Ronge Volcanic Belt. In: *Summary of Investigations 2003, Volume 2, Saskatchewan Geological Survey, Saskatchewan Industry Resources, Miscellaneous Report 2003-4.2, Paper B-2*, p. 12.
- Tourigny, G., 2003b. Preliminary Structural Study of the Gold-bearing Shear Zone System at the Seabee Mine, Northern Saskatchewan. In: *Summary of Investigations 2003, Saskatchewan Geological Survey, Saskatchewan Industry Resources, Miscellaneous Report 2003-4.2, Paper B-1*, p. 11.
- Uchida, E., Endo, S., Makino, M., 2007. Relationship between solidification depth of granitic rocks and formation of hydrothermal ore deposits. *Resour. Geol.* 57, 47–56. <https://doi.org/10.1111/j.1751-3928.2006.00004.x>.
- Van Schmus, W.R., Bickford, M.E., Macdonald, R., 1987. U-Pb geochronology in the Trans-Hudson Orogen, northern Saskatchewan, Canada. *Can. J. Earth Sci.* 24, 407–424.
- Whitney, D.L., Evans, B.W., 2010. Abbreviations for names of rock-forming minerals. *Am. Mineral.* 95, 185–187.
- Willson, J.R., 2010. *Minerals and Rocks*. BookBoon Press.
- Witvoet, L., 2023. Petrological and geochemical comparison of the Eisler intrusive suite and the Laonil Lake intrusion complex, Glennie Domain. Unpublished Msc Thesis. University of Saskatchewan, Northern Saskatchewan, p. 99.
- Wood, C.R., 2016. Structural study of the auriferous Santoy shear zone, northeastern Glennie domain, Saskatchewan. Unpublished MSc thesis. University of Regina, p. 154.
- Zane, A., Weiss, Z., 1998. A procedure for classifying rock-forming chlorites based on microprobe data. *Rend. Lincei* 9 (1), 51–56. <https://doi.org/10.1007/bf02904455>.
- Zang, W., Fyfe, W.S., 1995. Chloritization of the hydrothermally altered bedrock at the Igarapé Bahia gold deposit, Carajás, Brazil. *Miner. Deposita* 30, 30–38. <https://doi.org/10.1007/BF00208874>.
- Zhao, H., Wang, Q., Groves, D.I., Deng, J., 2019. A rare Phanerozoic amphibolite-hosted gold deposit at Danba, Yangtze Craton, China: significance to fluid and metal sources for orogenic gold systems. *Miner. Deposita* 54, 133–152. <https://doi.org/10.1007/s00126-018-0845-x>.
- Zwanig, H.V., 2000. Geochemistry and Tectonic Framework of the Kissynow Domain-Lynn Lake Belt Boundary (Part of NTS 63P/13). In: *Report of Activities 2000, Manitoba Industry, Trade and Mines, Manitoba Geological Survey*, pp. 91–96.